MARK2 variants cause autism spectrum disorder via the downregulation of WNT/β-catenin signaling pathway

Graphical abstract

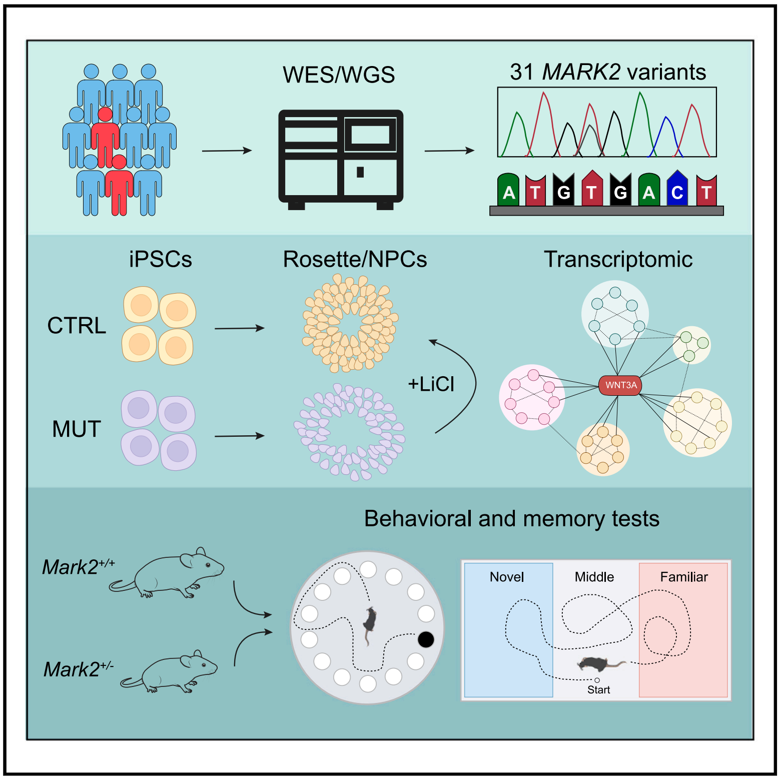

Authors

Maolei Gong, Jiayi Li, Zailong Qin, ..., Leonard Rappaport, Chang-Mei Liu, Xiaoli Chen

Correspondence

liuchm@ioz.ac.cn (C.-M.L.),
xiaolichen@pumc.edu.cn (X.C.)

MARK2 plays essential roles in the central nervous system. Here, we demonstrate the association between _MARK2_ variants, downregulated WNT/β-catenin signaling, and autism spectrum disorder (ASD) through the study of individuals with ASD and _Mark2_$^{+/-}$ mice.

Gong et al., 2024, The American Journal of Human Genetics *111*, 2392–2410
November 7, 2024
https://doi.org/10.1016/j.ajhg.2024.09.006

MARK2 variants cause autism spectrum disorder via the downregulation of WNT/β-catenin signaling pathway

Maolei Gong,[1,2,3,4,61] Jiayi Li,[5,6,61] Zailong Qin,[7,61] Matheus Vernet Machado Bressan Wilke,[8,61] Yijun Liu,[1,2,3,9] Qian Li,[1,2,3,9] Haoran Liu,[5] Chen Liang,[5] Joel A. Morales-Rosado,[10] Ana S.A. Cohen,[11,12] Susan S. Hughes,[12,13] Bonnie R. Sullivan,[12,13] Valerie Waddell,[14] Marie-José H. van den Boogaard,[15] Richard H. van Jaarsveld,[15] Ellen van Binsbergen,[15] Koen L. van Gassen,[15] Tianyun Wang,[16,17] Susan M. Hiatt,[18] Michelle D. Amaral,[18] Whitley V. Kelley,[18] Jianbo Zhao,[19] Weixing Feng,[19] Changhong Ren,[19] Yazhen Yu,[20] Nicole J. Boczek,[21] Matthew J. Ferber,[21] Carrie Lahner,[21] Sherr Elliott,[22] Yiyan Ruan,[23] Cyril Mignot,[24] Boris Keren,[24] Hua Xie,[5] Xiaoyan Wang,[25] Bernt Popp,[26,27] Christiane Zweier,[28,29] Juliette Piard,[30,31] Christine Coubes,[32] Frederic Tran Mau-Them,[33,34] Hana Safraou,[33,34] A. Micheil Innes,[35] Julie Gauthier,[36,37] Jacques L. Michaud,[37,38]

(Author list continued on next page)

Summary

Microtubule affinity-regulating kinase 2 (MARK2) contributes to establishing neuronal polarity and developing dendritic spines. Although large-scale sequencing studies have associated *MARK2* variants with autism spectrum disorder (ASD), the clinical features and variant spectrum in affected individuals with *MARK2* variants, early developmental phenotypes in mutant human neurons, and the pathogenic mechanism underlying effects on neuronal development have remained unclear. Here, we report 31 individuals with *MARK2* variants and presenting with ASD, other neurodevelopmental disorders, and distinctive facial features. Loss-of-function (LoF) variants predominate (81%) in affected individuals, while computational analysis and *in vitro* expression assay of missense variants supported the effect of *MARK2* loss. Using proband-derived and CRISPR-engineered isogenic induced pluripotent stem cells (iPSCs), we show that *MARK2* loss leads to early neuronal developmental and functional deficits, including anomalous polarity and dis-organization in neural rosettes, as well as imbalanced proliferation and differentiation in neural progenitor cells (NPCs). $Mark2^{+/-}$ mice showed abnormal cortical formation and partition and ASD-like behavior. Through the use of RNA sequencing (RNA-seq) and lithium treatment, we link *MARK2* loss to downregulation of the WNT/β-catenin signaling pathway and identify lithium as a potential drug for treating *MARK2*-associated ASD.

Introduction

Autism spectrum disorder (ASD) is a neurodevelopmental disorder (NDD) marked by difficulties in social communication and repetitive behaviors[1] that affects 0.7%–1.69% of children worldwide.[2,3] ASD shows high heritability, and 5%–30% of affected individuals have a Mendelian disorder.[4,5] Advances in genomic technologies have allowed the identification of over 300 risk ASD genes, including 100 high-confidence genes, through large-scale sequencing studies of autism cohorts.[6–9] Most genes relevant to ASD are highly intolerant to loss-of-function (LoF) variants in the human genome but are enriched for *de novo* variants in ASD individuals.[6–9]

Microtubule affinity-regulating kinase 2 (*MARK2*; MIM: 600526), also known as partitioning-defective 1b (PAR1b), is a member of the evolutionarily conserved PAR1/MARK serine/threonine kinase family,[10,11] and it plays essential roles in the central nervous system (CNS) via several cell biological functions.[12–17] In mouse primary hippocampal neurons *in vitro*, *Mark2* negatively modulates neuronal polarity and dendritic development,[13] and mouse neurons with *Mark2* depletion *in vivo* exhibit unpolarized dendritic overgrowth with multiplex rather than

[1]State Key Laboratory of Stem Cell and Reproductive Biology, Institute of Zoology, Chinese Academy of Sciences, Beijing, China; [2]Beijing Institute for Stem Cell and Regenerative Medicine, Beijing, China; [3]Institute for Stem Cell and Regeneration, Chinese Academy of Sciences, Beijing, China; [4]The Ninth Medical Center of PLA General Hospital, Beijing, China; [5]Department of Medical Genetics, Capital Institute of Pediatrics, Beijing, China; [6]Chinese Academy of Medical Sciences & Peking Union Medical College, Beijing, China; [7]Genetic and Metabolic Central Laboratory, Birth Defect Prevention Research Institute, Maternal and Child Health Hospital of Guangxi Zhuang Autonomous Region, Nanning, China; [8]Department of Clinical Genomics, Mayo Clinic, Rochester, MN, USA; [9]Savaid Medical School, University of Chinese Academy of Sciences, Beijing, China; [10]Department of Pathology, Microbiology & Immunology, Vanderbilt University Medical Center, Nashville, TN, USA; [11]Department of Pathology and Laboratory Medicine, Genomic Medicine Center, Children's Mercy-Kansas City, Kansas City, MO, USA; [12]The University of Missouri-Kansas City, School of Medicine, Kansas City, MO, USA; [13]Division of Clinical Genetics, Children's Mercy Kansas City, Kansas City, MO, USA; [14]Department of Neurology, Children's Mercy Kansas City, Kansas City, MO, USA; [15]Department of Genetics, University Medical Center Utrecht, Heidelberglaan 100, 3584 CX Utrecht, the Netherlands; [16]Department of Medical Genetics, Center for Medical Genetics, School of Basic Medical Sciences, Autism Research Center, Peking University Health Science Center, Beijing, China;

(Affiliations continued on next page)

Daniel C. Koboldt,[39] Odent Sylvie,[40,41] Marjolaine Willems,[42] Wen-Hann Tan,[43] Benjamin Cogne,[44,45] Claudine Rieubland,[28] Dominique Braun,[28] Scott Douglas McLean,[46,47] Konrad Platzer,[48] Pia Zacher,[49] Henry Oppermann,[48] Lucie Evenepoel,[50] Pierre Blanc,[51] Laïla El Khattabi,[52,53] Neshatul Haque,[54] Nikita R. Dsouza,[54] Michael T. Zimmermann,[54,55,56] Raul Urrutia,[57] Eric W. Klee,[8,58] Yiping Shen,[43,59] Hongzhen Du,[1,2,3] Leonard Rappaport,[60] Chang-Mei Liu,[1,2,3,9,*] and Xiaoli Chen[5,6,*]

single axons.[12] Additionally, downregulation of *Mark2* by *in utero* electroporation inhibits neuronal migration in the mouse cortex,[15] and unpolarized neurons accumulate in the intermediate zone (IZ) of the developing cerebral cortex.[15] Recently, Zhou et al. performed an integrated analysis of the largest set of sequencing data from 42,607 individuals with ASD and identified *MARK2* as a moderate-risk gene for ASD.[18] However, the clinical features and variant spectrum of affected individuals with ASD with *MARK2* variants (*MARK2*-associated ASD), as well as the pathophysiological effect and molecular mechanism of *MARK2* variants on human neurogenesis, especially on human NPCs/stem cells, remain unclear.

Herein, we describe a cohort of 31 individuals with clinically relevant *MARK2* variants, mostly LoF variants (25/31), who were gathered through GeneMatcher.[19] All affected individuals presented with ASD and other NDD features, and the majority have distinctive facial features. Using proband-derived induced pluripotent stem cells (iPSCs) combined with CRISPR-engineered isogenic iPSCs, we revealed the cellular phenotypes and transcriptomic profiles of mutant neural progenitor cells (NPCs). Furthermore, in experiments with *Mark2*$^{+/-}$ (HET) mice, we recapitulated the pathophysiological deficits observed in mutant NPCs and the ASD-related behaviors presented by affected individuals. Importantly, we identified downregulation of the WNT/β-catenin signaling pathway as the molecular mechanism of *MARK2* variant, and lithium reversed abnormal cellular phenotypes of mutant NPCs cells both *in vitro* and *in vivo* via re-activating the WNT/β-catenin signaling pathway.

Material and methods

Ethics statement

The study was approved by the ethics committees of the respective institutions, including the Capital Institute of Pediatrics (SHERLL2021008), Mayo Clinic (IRB#19–003389), and Maternal and Child Health Hospital of Guangxi Zhuang Autonomous Region (2017-3-11). This international individual cohort carrying the *MARK2* variant was recruited by the GeneMatcher data sharing platform.[19] Informed consent was obtained from all participants or proband's legal guardians prior to study inclusion. Additional consent for the publication of photos was optional. The detailed

[17]Neuroscience Research Institute, Peking University, Key Laboratory for Neuroscience, Ministry of Education of China & National Health Commission of China, Beijing, China; [18]HudsonAlpha Institute for Biotechnology, Huntsville, AL, USA; [19]Department of Neurology Beijing Children's Hospital, Capital Medical University, Beijing, China; [20]Department of Pediatrics, Beijing Tiantan Hospital affiliated with Capital University of Medical Sciences, Beijing, China; [21]Department of Laboratory Medicine and Pathology, Genomics Laboratory, Mayo Clinic, Rochester, MN, USA; [22]Departments of Neurology and Pediatrics, Institute of Human Genetics and Weill Institute for Neurosciences, University of California, San Francisco, San Francisco, CA, USA; [23]Guangxi Clinical Research Center for Pediatric Diseases, The Maternal and Child Health Care Hospital of Guangxi Zhuang Autonomous Region, Nanning, China; [24]APHP Sorbonne Université, Département de Génétique, Hôpital Pitié-Salpêtrière et Hôpital Trousseau, Centre de Référence Déficiences Intellectuelles de Causes Rares, Paris, France; [25]Department of Children's Nutrition Research Center, Affiliated Children's Hospital of Capital Institute of Pediatrics, Beijing, China; [26]Institute of Human Genetics, University of Leipzig Hospitals and Clinics, Leipzig, Germany; [27]Berlin Institute of Health at Charité-Universitäts medizin Berlin, Center of Functional Genomics, Hessische Straße 4A, Berlin, Germany; [28]Department of Human Genetics, Inselspital, Bern University Hospital, University of Bern, Bern, Switzerland; [29]Institute of Human Genetics, University Hospital Erlangen, Friedrich-Alexander Universität Erlangen-Nürnberg, Erlangen, Germany; [30]Centre de Génétique Humaine, Centre Hospitalier Régional Universitaire, Université de Franche-Comté, Besançon, France; [31]UMR 1231 GAD, Inserm, Université de Bourgogne Franche Comté, Dijon, France; [32]Département de Génétique Médicale, Maladies Rares et Médecine Personnalisée Hôpital Arnaud de Villeneuve, 34295 Montpellier Cedex, Dijon, France; [33]UF6254 Innovation en Diagnostic Genomique des Maladies Rares, Dijon, France; [34]Inserm UMR1231 GAD, 21000 Dijon, France; [35]Department of Medical Genetics and Pediatrics and Alberta Children's Hospital Research Institute, Cumming School of Medicine, University of Calgary, Calgary, Alberta, Canada; [36]Molecular Diagnostic Laboratory, Centre Hospitalier Universitaire Sainte-Justine, Montréal, QC, Canada; [37]Department of Pediatrics, Université de Montréal, Montréal, QC, Canada; [38]CHU Sainte-Justine Research Center, Montreal, QC, Canada; [39]The Institute for Genomic Medicine, Nationwide Children's Hospital, Columbus, OH, USA; [40]Service de Génétique clinique, CHU Rennes, ERN ITHACA, Rennes, France; [41]University Rennes, CNRS, INSERM, IGDR (Institut de Génétique et développement de Rennes), UMR 6290, ERL U1305, Rennes, France; [42]Medical Genetic Department for Rare Diseases and Personalized Medicine, Reference Center AD SOOR, AnDDI-RARE, Inserm U1298, INM, Montpellier University, Centre Hospitalier Universitaire de Montpellier, Montpellier, France; [43]Division of Genetics and Genomics, Boston Children's Hospital, Harvard Medical School, Boston, MA, USA; [44]Nantes Université, CHU Nantes, Service de Génétique Médicale, Nantes, France; [45]Nantes Université, CHU Nantes, CNRS, INSERM, l'institut du thorax, Nantes, France; [46]Division of Clinical Genetics, The Children's Hospital of San Antonio, San Antonio, TX, USA; [47]Department of Molecular and Human Genetics, Baylor College of Medicine, Houston, TX, USA; [48]Institute of Human Genetics, University of Leipzig Medical Center, Leipzig, Germany; [49]Epilepsy Center Kleinwachau, Dresden-Radeberg, Germany; [50]Centre de Génétique Humaine, Cliniques Universitaires Saint-Luc, Université Catholique de Louvain, Avenue Hippocrate 10-1200, Brussels, Belgium; [51]Sorbonne Université, Department of Medical Genetics, APHP, Pitié-Salpêtrière hospital, Paris Brain Institute-ICM, Laboratoire SeqOIA-PFMG2025, Paris, France; [52]Department of Medical Genetics, APHP, Armand Trousseau and Pitié-Salpêtrière hospitals, Brain Development team, Paris Brain Institute-ICM, Sorbonne Université, Paris, France; [53]Laboratoire SeqOIA-PFMG2025, Paris, France; [54]Bioinformatics Research and Development Laboratory, Linda T. and John A. Mellowes Center for Genomic Sciences and Precision Medicine, Medical College of Wisconsin, Milwaukee, WI, USA; [55]Department of Biochemistry, Medical College of Wisconsin, Milwaukee, WI, USA; [56]Clinical and Translational Sciences Institute, Medical College of Wisconsin, Milwaukee, WI, USA; [57]Department of Surgery, Medical College of Wisconsin, Milwaukee, WI, USA; [58]Department of Quantitative Health Sciences, Mayo Clinic, Rochester, MN, USA; [59]SynerGene Education, Hejun College, Huichang Jiangxi, China; [60]Division of Developmental Medicine, Boston Children's Hospital, Harvard Medical School, Boston, MA, USA

[61]These authors contributed equally

*Correspondence: liuchm@ioz.ac.cn (C.-M.L.), xiaolichen@pumc.edu.cn (X.C.)

https://doi.org/10.1016/j.ajhg.2024.09.006.

clinical information was recorded by the referring clinician. Sample collection and consent was in accordance with the tenets of the Declaration of Helsinki.

Detection of *MARK2* variants

MARK2 variants were detected in peripheral blood samples by proband-only whole exome-sequencing (WES) or Trio whole-genome sequencing (WGS) combined with Sanger sequencing. WES was performed with commercial exome capture kits and was followed by sequencing on the Illumina NovaSeq 6000 platform.

Variants were annotated based on transcript GenBank: NM_001039469.3 using the reference human genome GRCh37(hg19) version. The inheritance of *MARK2* variants was confirmed in all families by Sanger sequencing. Two pairs of primers were designed to exclude amplification bias during PCR. For missense variants, only those that were predicted as deleterious variants by more than 2 software programs (PolyPhen2, SIFT, CADD, REVEL) were included. The pathogenicity of each candidate mutation was classified according to the 2015 guidelines of American College of Medical Genetics and Genomics (ACMG).[20] The identities of biological parents were confirmed for all affected individuals before using the PS2 criteria. The criteria for PP3[21] and PVS1[22] evidence were modified based on the ACMG guidelines.

Expression vector construction, cell culture, transient transfection

Two splicing variants (c.337+1G>T, c.1514+2T>G) and 6 missense variants (p.Ala80Val [c.239C>T], p.Gly135Arg [c.403G>A], p.Phe194Ser [c.581T>C], p.Arg302Gln [c.905G>A], p.Val752Ala [c.2255T>C], p.Arg764Pro [c.2291G>C]) were chosen for *in vitro* transient transfection and functional assay. For splicing variants, 2 genomic fragments covering wild-type (WT) *MARK2* c.337+1G allele (1039bp, see Table S1 for primers) or covering the c.1514+2T allele (2441bp, see Table S1 for primers) were amplified by standard PCR or overlap-extension PCR and then cloned into the pcDNA3.1 vector. For missense variants, full-length WT *MARK2* cDNA (2367bp, GenBank: NM_001039469.3) was synthesized and cloned into pCMV-EGFP-Neo vector using 2 primers containing KpnI and AgeI restriction enzyme sites. The mutant vectors were constructed by site-specific mutant primers and overlap-extension PCR (Table S1). All vectors were verified by sequencing.

Human embryonic kidney 293T (HEK 293T) cells and HeLa cells (ATCC) were grown in minimum Eagle's medium supplemented with 10% fetal bovine serum and antibiotics. The cells were grown to 70%–90% confluence before transient transfection (Lipofectamine 2000 reagent, Invitrogen). Forty-eight h later, transfected cells were washed twice with cool 1× PBS and then collected for RNA extraction (splicing variants), protein lysis, and western blotting (missense variants). Total RNA was extracted (TRIzol, Omega) and reverse transcribed into cDNA (SuperScript reverse transcription kit, Thermo) followed by standard PCR (Table S1 for primers). The PCR products were visualized on a 2% agarose gel and then purified for Sanger sequencing.

Model construction and calculation

The protein accession number GenBank: NP_001034558.2 was used. The structure of the kinase-associated domain 1 (KA1) of human MARK2 is unknown, but the experimental structures of all human KA1 domains are sufficiently identical (71%) to generate a high-confidence KA1 model through homology-based methods.[23] The structures of the kinase and ubiquitin-associated (UBA) domains of MARK2 have been experimentally determined (PDB ID: 1zmu).[24] These independently generated models were integrated using information from AlphaFold2.[25]

Regions of the protein that do not adopt secondary structures and are likely to be intrinsically disordered regions (IDRs) were loop modeled using Modeller version 10.2.[26] The combined 3D model was used for visualization and structure-based calculations of stability alterations due to genomic variants.[27] We assessed short linear motifs (SLiMs) of each missense variant by programmatically accessing the web of Eukaryotic Linear Motif (ELM, http://elm.eu.org).[28] In addition, we calculated the local stability (ΔΔGfold) and the balance of favorable and unfavorable local contacts, termed frustration for missense variants.

Generation of iPSC lines from 2 affected individuals

Peripheral blood mononuclear cells (PBMCs) were reprogrammed into iPSCs using a CytoTune-iPS 2.0 Sendai Reprogramming Kit (Invitrogen) as we previously reported.[29] In brief, PBMCs were seeded in 12-well plates and cultured for 14 days in PBMC medium. Then, 2.5×10^5 PBMCs were infected with Sendai virus and cultured for 48 h at 37°C. Then, the infected cells were added to mouse embryonic fibroblast (MEF) feeders in iPSC medium. After 2 weeks, individual iPSC colonies were picked manually, transferred to Matrigel (Corning)-coated dishes, and maintained in mTeSR medium (Stem Cell Technologies). Routine testing revealed that the cells were mycoplasma negative. After more than 10 passages, the characteristics of the iPSCs, including their pluripotency and genomic background, were analyzed. For pluripotency analysis, we performed alkaline phosphatase (AP) staining and immunofluorescence (IF) staining and assessed teratoma formation. To evaluate genomic background, we performed karyotyping, short tandem repeat (STR) site analysis, and array comparative genomic hybridization (CGH) to confirm that the genomes were identical. Two iPSC lines from 2 normal unrelated adults we previously reported were used as control iPSCs.[29] Meanwhile, 2 isogenic iPSCs were generated using CRISPR-Cas9 gene editing engineering to delete the KA1 domain of *MARK2* with heterozygous status, and the top 6 off-target genes sorted by cutting frequency determination (CFD) off-target score were tested (CRISPR-Del1 and CRISPR-Del2, see Table S1 for guide RNA [gRNA] primers).

Neural differentiation of iPSCs

iPSCs were maintained on Matrigel (BD Biosciences) in mTeSR1 medium (StemCell Technologies) and performed for neural differentiation. Between passages 12 and 30, iPSCs were used for neural differentiation as previously described with minor modifications.[30] In brief, 30,000 iPSCs were used for embryoid bodies (EBs) culture, and after 24 h, EBs were planted to poly-L-ornithine/laminin-coated plates. Then, EBs were grown in a 1:1 mixture of N2- and B27-containing media (N1 medium) supplemented with EGF2 (Gibco, 1 mg/mL), Noggin (BD Biosciences, 250 ng/mL), SB431542 (Selleck, 10 mM), and Laminin (Gibco, 0.5 mg/mL) for 10 days. For neural differentiation, N1 medium was changed to a 1:1 mixture of N2- and B27-containing media (N2 medium) supplemented with FGF1 (Gibco, 1 mg/mL), EGF2 (Gibco, 1 mg/mL), BDNF (Gibco, 100 μg/mL), and Laminin (Gibco, 0.5 mg/mL) for another 3 days. For neurospheres, EBs were grown in suspension culture in DMEM/F12 supplemented with 1× N2 (Gibco), 1× nonessential amino acids (Gibco), Knockout Serum Replacement (Gibco), and Mercaptoethanol (Sigma, 25 nM) for 5 days.

RNA sequencing

Two iPSC-derived NPCs of P19 were used for this experiment. Total RNA was extracted from iPSC-derived NPCs with TRIzol reagent (Invitrogen) according to the manufacturer's protocol. Two micrograms of RNA were used for sequencing library generation using the NEBNext Ultra RNA Library Prep Kit (NEB). The cDNA library was preliminarily quantified using a Qubit RNA Assay Kit (Thermo Fisher Scientific) and then diluted to 1 ng/μL. Insert size was assessed using the Agilent Bioanalyzer 2100 system (Agilent Technologies) and quantified using StepOnePlus RT-PCR. The cDNA library was sequenced with the Illumina HiSeq 2500 platform (Annoroad) to generate 150-bp paired-end sequence reads. Read counts and FPKM for genes were extracted using the standard RNA sequencing (RNA-seq) analysis flowchart. Briefly, Fastq was used to assess sequencing quality control and remove the reads containing adapter sequences.[31] Reads were mapped to the GRCh38 version of the human genome and transcriptome with Salmon (v.1.0.0, SAF Pattern). Normalization and differential gene expression were performed with DESeq2 Bioconductor package (https://github.com/thelovelab/DESeq2) with the R statistical programming environment (v.4.2.2). Genes were identified as significant genes with a p value <0.05 and an absolute value of $\log_2^{\text{fold change}} > 1.5$ and were used for gene function and pathway enrichment analyses, including Gene Ontology (GO) analysis and gene set enrichment analysis (GSEA) with clusterProfiler Bioconductor package (https://github.com/YuLab-SMU/clusterProfiler).

RT-quantitative PCR validation

Total RNA from iPSC-derived NPCs was reverse transcribed into cDNA using the transcript one-step gDNA removal and cDNA synthesis kit (TransGen Biotech), and the diluted (1:100) cDNA was used as a template for qPCR. qPCR was performed on a 7500 FAST Real-Time PCR system (Life Technologies) using an SYBR select master mix kit with specific primers. Relative gene expression was analyzed by the $2^{-\Delta\Delta CT}$ method, and GAPDH or actin was used as an endogenous control. The RT-qPCR primers are listed in Table S1.

Western blot analysis and IF staining

Total protein was extracted from cells or tissue using RIPA buffer containing 10 mM PMSF (Beyotime Biotechnology), and the protein concentration was determined using a BCA protein assay kit (Beyotime Biotechnology). The membranes were blocked in 5% milk in TBST (0.1% Tween 20) and incubated with primary antibodies at 4°C overnight. The membranes were then washed in TBST for 10 min 3 times and incubated with secondary antibodies at room temperature for 2 h. An ECL system (Pierce) and Tanon-5200 Chemiluminescent Imaging System (Tanon) were used for signal detection.

Brains of embryonic day (E) 18.5 mice were postfixed with 4% paraformaldehyde (PFA) overnight and then dehydrated with 30% sucrose. The tissues were embedded and cut into 35-μm-thick cryosections. For IF staining, sagittal cortex slices or cells were permeabilized (0.5% Triton X-100 and 3% BSA in PBS) for 15 min and blocked (0.3% Triton X-100 and 3% BSA in PBS) for 1 h at room temperature. Next, the slices or cells were incubated with relevant primary antibodies (0.3% Triton X-100 and 3% BSA in PBS) overnight at 4°C. The samples were incubated with AlexaFluor 488-, 568-, 594- or 647-conjugated secondary antibodies (1:500), and nuclei were counterstained with DAPI (1:1,000). Antibody categories are listed in Table S2.

Microscopy and analysis of NPCs

Confocal images were acquired using Zeiss LSM880 confocal microscopes and analyzed by ZEN software.

Mouse lines

The animal experiments were approved by the Laboratory Animal Center, Institute of Zoology, Chinese Academy of Sciences and were performed in accordance with relevant Chinese regulations. *Mark2*$^{+/-}$ mice were generated by Cyagen Biosciences (China) using double gRNA CRISPR-Cas-mediated genome engineering to delete exons 2–17 of *Mark2*. gRNA primers are listed in Table S1. All mice were bred in a specific-pathogen-free facility on a 12-h light/dark cycle, and food and water were available *ad libitum*.

BrdU incorporation analysis

BrdU (Sigma) was administered by intraperitoneal injection at a dose of 100 mg/kg body weight of the mother mouse. Brains were harvested 1 h later for subsequent analysis. Antibody categories are listed in Table S2.

Behavioral and memory tests

Female mice have hormonal cycles that may potentially complicate the results. To avoid the effect of hormone, only male mice aged 8–12 weeks ($n \geq 8$ per group) were used for behavioral and memory tests. All tests were performed between 09:00 and 17:00. Videos of the behavioral tests were analyzed by EthoVision XT 14 (Noldus). Behavioral tests included open field, elevated plus maze, three-chamber, novel object recognition, marble burying, grooming, Y-maze, Barnes maze, and Morris water maze (see supplemental information for more details).

In vitro and *in vivo* rescue assays

For the *in vitro* rescue assay, either 0.7 mM LiCl (Sigma) or 100 ng/mL recombinant human WNT3A (rhWNT3A; R&D Systems) were supplemented in the culture media from the first day of differentiation process. The rescue efficacy was evaluated at specific time points by western blot and IF.

For the *in vivo* rescue assay, 6–8-month-aged female WT mice were allowed to mate freely with male HET mice. Once the vaginal plug was observed the following morning, the drinking water was replaced with clean drinking water containing LiCI (4.5 mg/L). The brains of fetal mice were collected at E18.5 for IF screening.

Statistical analysis

Data are presented as the mean ± standard error of the mean (SEM) unless otherwise indicated. At least 3 biological replicates were performed for each group. For statistical analyses, unpaired Student's t tests were performed using GraphPad Prism software. Statistical significance was defined as $^*p < 0.05$, $^{**}p < 0.01$, and $^{***}p < 0.001$.

Results

Variant spectrum and clinical features of *MARK2*-related ASD

We utilized the GeneMatcher data sharing platform[19] to assemble this international cohort. A total of 29 distinct *MARK2* variants (Figure 1A; Table S3) were detected in 31 individuals, including 2 reported individuals from the

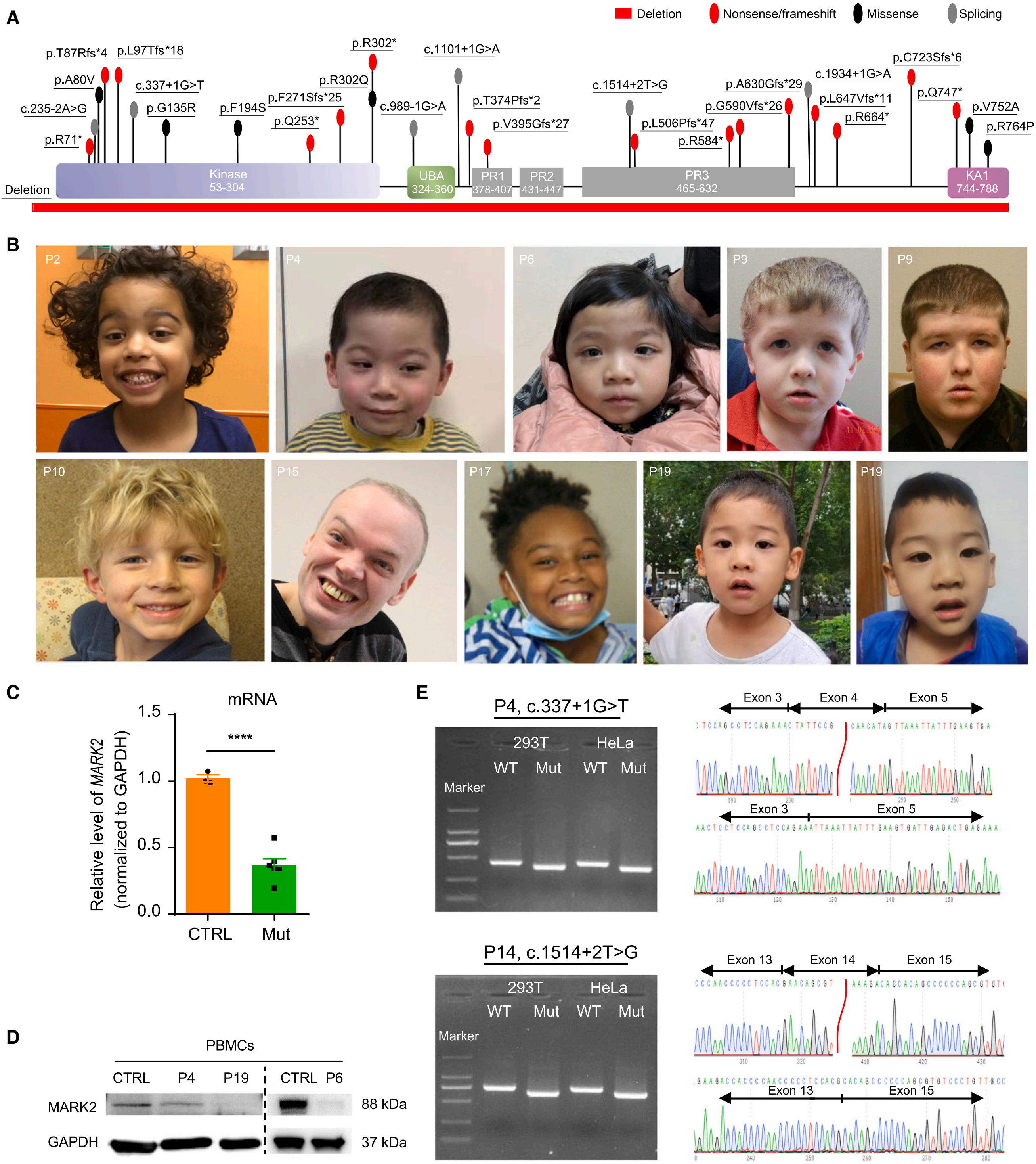

Figure 1. Overview of *MARK2* variants and associated phenotypes

(A) Locations of variants in functional domains of MARK2 predicted by UniProt are shown. p.Arg302* and p.Gln747* are recurrent variants that occurred in 2 individuals. Kinase, protein kinase domain; UBA, ubiquitin associated; PR, polar residue; KA1, kinase-associated domain 1.

(B) Facial photos of 8 affected individuals. Ages at the time of photograph are P2, 5 years and 4 months; P4, 4 years and 2 months; P6, 3 years and 1 month; P9 left, 4 years; P9 right, 11 years; P10, 8 years; P15, 46 years; P17, 7 years and 7 months; P19 left, 4 years; P19 right, 4 years and 7 months.

(C and D) The mRNA expression (C) and protein accumulation (D) of *MARK2* in the PBMCs from 3 affected individuals (Mut: P4, P6, P19). Both mRNA and protein levels were normalized to GAPDH levels and compared with those of age-matched healthy children (CTRL). The data of at least 3 independent experiments were analyzed by Student's t test, *$p < 0.05$.

(legend continued on next page)

Deciphering Developmental Disorders (DDD) study.[18] Notably, 27 of 29 variants were not reported in the gnomAD and our in-house database. Two variants recurred in independent individuals from different ethnicities and laboratories (p.Arg302* [c.904C>T] in P8 and P12, p.Gln747* [c.2239C>T] in P20 and P24). Variant spectrum (Table 1) comprised 25 LoF variants (nonsense/frameshift/splicing) (81%) and 6 missense variants (19%). All LoF variants led to the loss of the entire KA1. Among 25 LoF variants, 16 (64%) were *de novo*, and 4 (16%) were paternally inherited. All missense variants were *de novo*. Three individuals presented variants at the same position (Arg302), including 2 LoF variants (p.Arg302*) and 1 missense variant (p.Arg302Gln). No other clinically relevant or pathogenic variants were detected in affected individuals. All variants were classified as likely pathogenic or pathogenic according to ACMG/AMP criteria.[20]

The detailed clinical features associated with the *MARK2* variants are summarized (Tables 1 and S3). The ages of individuals in our cohort ranged from 2 to 46 years old, with no observed sex difference (13 females and 18 males). The majority of affected individuals were described as having distinctive and recurrently noted features that included a narrow face, abnormal or broad forehead, downslanting palpebral fissures, and large or dysplastic ears. Representative images of 8 individuals are shown (Figure 1B). Eye problems, including hyperopia, myopia, astigmatism, strabismus, ptosis, and visual processing difficulties, were observed in 39.3% of the individuals (11/28). All individuals except 1 (P8) presented with ASD (30/31). Other NDDs were common within the cohort, including intellectual disability/developmental delay (100%), speech-language problems (100%), seizure/epilepsy (46%), motor delay (62%), and behavior disorders (74%). Language regression was reported in 41% (9/22) of individuals with 4 individuals still presenting language regression (P6, P19, P8, and P9) over time. The high penetrance of NDDs suggested that *MARK2* is associated with ASD with NDD comorbid features.

To assess the consequence of LoF variants, *MARK2* levels from PBMCs of 3 affected individuals (c.337+1G>T variant in P4, p.Phe271Serfs [c.812delT] in P6, and p.Cys723Serfs [c.2168_2169delGC] variant in P19) were measured for both mRNA and protein *in vivo* (Figures 1C and 1D). As shown, the mRNA and protein expression of *MARK2* were significantly lower in affected individuals (Mut) than in the control group (CTRL). We also validated the splicing effects of 2 canonical splicing variants (c.337+1G>T variant in P4 and c.1514+2T>G variant in P14) *in vitro* using a minigene assay (Figure 1E). The transcripts of these *MARK2* variants (Mut) were shorter than that of WT. Sequencing and online alignment of the RT-PCR products revealed 1 exon skipping event in the transcript, with a 49-bp deletion in the c.337+1G>T variant and a 98-bp deletion in the c.1514+2T>G variant. Both *in vivo* and *in vitro* experiments confirmed *MARK2* loss due to LoF variants.

Structural modeling and *in vitro* expression assay reveal that missense variants in key domain of *MARK2* cause protein destabilization

MARK2 contains 5 domains, including kinase, KA1, UBA, and 3 polar residue domains.[10] All missense variants identified in our cohort (p.Ala80Val, p.Gly135Arg, p.Phe194Ser, p.Arg302Gln, p.Val752Ala, p.Arg764Pro) were clustered in the kinase or KA1 (Figure 1A) domains and involved the highly evolutionary conserved residues across species from *Drosophila* to human (Figure 2A). We analyzed the missense mutation tolerance map (https://stuart.radboudumc.nl/metadome/dashboard) by extracting missense and synonymous variants from the gnomAD database (gnomAD v.2.1.1, https://gnomad.broadinstitute.org/)[32] and found both the kinase and KA1 domains are intolerant to missense mutations (Figure S1).

Information from evolutionary couplings indicates that the tail and KA1 domains fold together with the kinase domain,[33] and 6 missense variants are within this structured dual domain (Figure 2B). Amino acids in the kinase domain are expected to have a balanced frustration so that the kinase can move as part of the normal cycle of ATP/ADP exchange and substrate access. Further, the effects of 6 variants on stability, frustration, binding motifs, and biochemical role in the enzyme, the altered 3D domain structure, or SLiMs were shown in Tables S4 and S5. The fraction of highly frustrated interactions around Ala80 is comparable, and the $\Delta\Delta G_{fold}$ of the p.Ala80Val variant shows little to no change. However, the backbone of Ala80 and Met129, the gatekeeper residues of the kinase fold, form a hydrogen bond, as they are in adjacent β-strands. The degree of freedom of Met129 may be restricted by the comparatively bulkier side chain of Val80, indirectly and negatively affecting the catalytic function via a dynamic mechanism. Both Gly134 and Gly135 are in the kinase domain near the KA1 binding surface and solvent exposed. The $\Delta\Delta G_{fold}$ of p.Gly135Arg variant is highly unfavorable, suggesting that the variant destabilizes the kinase domain. Gly135 is also positioned in the ATP-binding pocket, and the introduction of a large polar amino acid to the vicinity is likely to dysregulate nucleoside binding. p.Gly135Arg variant introduces a different sequence motif for cleavage. If this motif is recognized, it could represent the manner in which MARK2 is inactivated. Phe194 is located in the N-terminal base of the kinase activation loop and is a key residue in the classic Asp-Phe-Gly (DFG) motif. Phe194 anchors the activation

(E) Minigene assays of 2 splicing variants (P4: c.337+1G>T; P14: c.1514+2T>G). RT−PCR products from HEK 293T and HeLa cells transfected with either the wild-type (WT) or mutant (Mut) pcDNA3.1 vector were separated by electrophoresis (left). M, DNA marker; the sizes of the bands are 2,000, 1,000, 750, 500, 250, and 100 bp. Sequencing of the RT-PCR products (right) show c.337+1G>T variant results in a 49-bp deletion, while the c.1514+2T>G variant results in a 98-bp deletion.

Table 1. The detailed clinical features and variant spectrum of 31 individuals with *MARK2* variants

Clinical features[a]	age at measurements (years)	2–46
	sex (male/female)	18/13
	autism spectrum disorder	30/31 (96.8%)
	intellectual disability/developmental delay	29/29 (100%)
	speech-language problems	31/31 (100%)
	behavior abnormalities (ADHD, aggression and anxiety, depression)	20/27 (74.1%)
	motor delay	18/29 (62.1%)
	brain EEG	8/15 (53.3%)
	seizure/epilepsy	13/28 (46.4%)
	language regression	9/22 (40.9%)
	visual impairment	11/28 (39.3%)
	genital malformation in male	6/18 (33.3%)
	muscle or other information	9/28 (32.1%)
Genomic variant spectrum[b]	LoF variant	25/31 (81%)
	LoF variant without KA1 domain	25/31 (81%)
	de novo	16/25 (64%)
	parental inherited	4/25 (16%)
	unknown	5/25 (20%)
	missense variant	6/31 (19%)
	de novo	6/6 (100%)

[a] Key features with frequency >30% were summarized. Some feature information wasn't available for affected individuals, causing inconsistent denominators.
[b] Variants classified as pathogenic/likely pathogenic were recruited.

loop within the kinase domain by hydrophobic interaction, rendering optimum flexibility to the activation loop. Two sequence motifs were gained in the p.Phe194Ser variant, 1 for phosphorylation by CK1 and another for glycosaminoglycan attachment. Thus, there is also potential for this genomic variant to introduce different regulatory dynamics into the enzyme, particularly given its proximity to known phosphorylation sites such as Ser197, Thr201, and Thr208. Arg302 is in the C-terminal helix of the kinase domain, which connects to the UBA domain. Arg302 was solvent exposed in our model and formed a hydrogen bond network among the Asp276 residue of the kinase, the N-terminal loop connected to the UBA domain, and additional N-terminal residues of the kinase. The frustration level indicated that p.Arg302Gln resulted in destabilization, while the $\Delta\Delta G_{fold}$ indicated that this variant caused stabilization. According to structural analysis, the hydrogen bond between Gln302 and Asp276 was preserved in the mutated protein. Thus, p.Arg302Gln can be tolerated but may also have allosteric effects on the kinase, as we have previously reported.[34] Val752 lies in the core of the hydrophobic interaction between the KA1 and tail domains. p.Val752Ala is a cavity-forming variant that may destabilize the hydrophobic core, potentially disrupting the formation of this autoregulatory domain. Similar to the kinase domain variants that destabilize KA1 interactions, p.Arg764Pro lies in the same interaction region and is therefore a reciprocal change with similar instabilities induced in the kinase-autoregulatory interaction. The $\Delta\Delta G_{fold}$ value suggested that p.Val752Ala is destabilizing, leaving a weaker autoinhibition state. All 6 missense variants were predicted to result in loss of kinase catalytic function; we then hypothesize that the missense alterations observed in this cohort could lead to MARK2 destabilization or inactivation.

In order to test this hypothesis, we constructed and transfected pCMV-Neo-MARK2 vectors into HEK 293T cells and analyzed the exogenous mutant MARK2. As shown in Figures 2C and 2D, 6 mutant cells resulted in significantly lower MARK2 accumulation compared with WT cells. Among them, the p.Gly135Arg variant had the lowest MARK2 accumulation. These *in vitro* data suggested that missense variants in the kinase and KA1 domain can result in decreased protein accumulation due to MARK2 destabilization and thereby phenocopy *MARK2* loss arising from LoF variants.

MARK2 variants lead to anomalous polarity in iPSC-derived neural rosettes and imbalanced proliferation and differentiation in iPSC-derived NPCs

Although the roles of *Mark2* in mouse mature neurons are recognized, such as controlling hippocampal neuronal

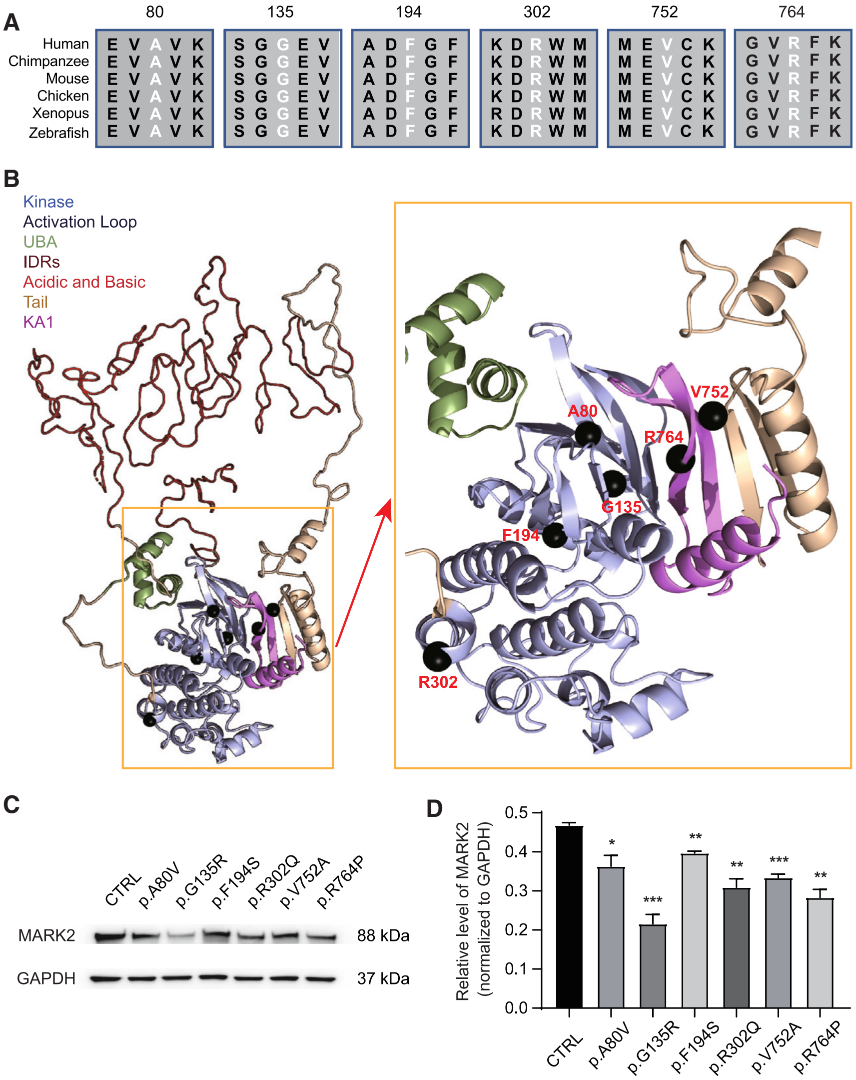

Figure 2. Structural modeling of six MARK2 missense variants

(A) Alignment of the protein sequences for 6 MARK2 missense variants across species from zebrafish to humans.

(B) 3D structural models of MARK2 missense variants. The protein domains of MARK2 are shown in different colors. The 3D structures of the non-intrinsically disordered regions (non-IDRs) were used to compute the changes in structural stability due to genomic variation. Amino acids in the IDRs are shown in a disordered configuration; we expect that any individual configuration of the IDRs would be an inadequate representation of their diverse dynamics. The locations of the 6 missense variants are marked by black spheres. Four variants in the kinase domain (p.A80V, p.G135R, p.F194S, p.R302Q) and 2 variants in the KA1 domain (p.V752A, p.R764P) were all predicted to locate in the activation loop.

(C and D) Representative western blot image (C) and quantification analysis of exogenous MARK2 accumulation that were normalized by total GAPDH levels (D). Human HEK 293T cells transfected with wild-type (CTRL) or mutant EGFP-*MARK2*-Neo vectors were lysed. The data of at least 3 independent experiments were analyzed by Student's t test $*p < 0.05$, $**p < 0.01$ and $***p < 0.001$.

polarity and migration, dendritic spinal formation,[12–17] the early neuronal development phenotypes, and fundamental mechanism of *MARK2* variant in human are unclear. To clarify it, we generated 2 mutant iPSCs from the PBMCs of 2 affected individuals (p.Cys723Serfs from P19 and p.Phe271Serfs from P6), 2 control iPSCs from healthy males (CTRL1 and CTRL2) (Figures 1A and S2B), and 2 isogenic mutant iPSCs (CRISPR-Del1 and CRISPR-Del2). Each iPSC donor has at least 2 clones. Their pluripotencies (SOX2, OCT3/4, and NANOG, Figure S2A), karyotypes (Figure S2B), and differentiation abilities to the 3 germ layers (Figure S2C) were confirmed.

Neural rosettes develop from the self-organized and differentiated iPSCs and present radial arrangements of neuroepithelial cells with 1 central lumen resembling a developing neural tube.[35] The key morphology of neural rosette includes intercalation, constriction, polarization, elongation, and lumen formation.[35,36] Considering the role of *MARK2* in neuronal polarity,[12] we co-stained neural rosettes using specific antibodies for neuronal marker (TUJ1) and polarity marker (ZO1) (Figure 3A). First, we found that both mutant and CRISPR-Del neural rosettes were different from CTRLs (Figures 3A, 3B, and 3D, yellow dotted loop), with the diameters of the rosettes being significantly increased (Figures 3A, 3B, and S3A) and the number of rosettes per 100 cells being significantly decreased (Figure S3B), suggesting few and unstable, loose neural rosette formation after *MARK2* loss. CTRL rosettes exhibited well-defined self-organization characterized by apical-basal polarity and constriction. TUJ1 staining revealed radial distribution surrounding the inner lumen, while ZO1 staining demonstrated clear localization within the inner lumen, which is consistent with previous reports (Figure 3A).[36] In contrast, both mutant and CRISPR-Del rosettes exhibited loose structure, characterized by imperfectly self-organized TUJ1 staining and degraded ZO1 staining, along with the absence of an inner lumen (Figure 3A). These results demonstrated that *MARK2* loss led to aberrant polarity of neuroepithelial cells, forming dis-organized, few, and loose-structured neural rosettes. Further comparation of the diameters of different iPSC-derived neurospheres revealed a significant reduction in size in mutant and CRISPR-Del groups (Figures 3C and S3D). We then checked the activated NPC population in rosettes using SOX1[37] and observed a significant decrease in the number of $SOX1^+$ cells within mutant and isogenic neural rosettes

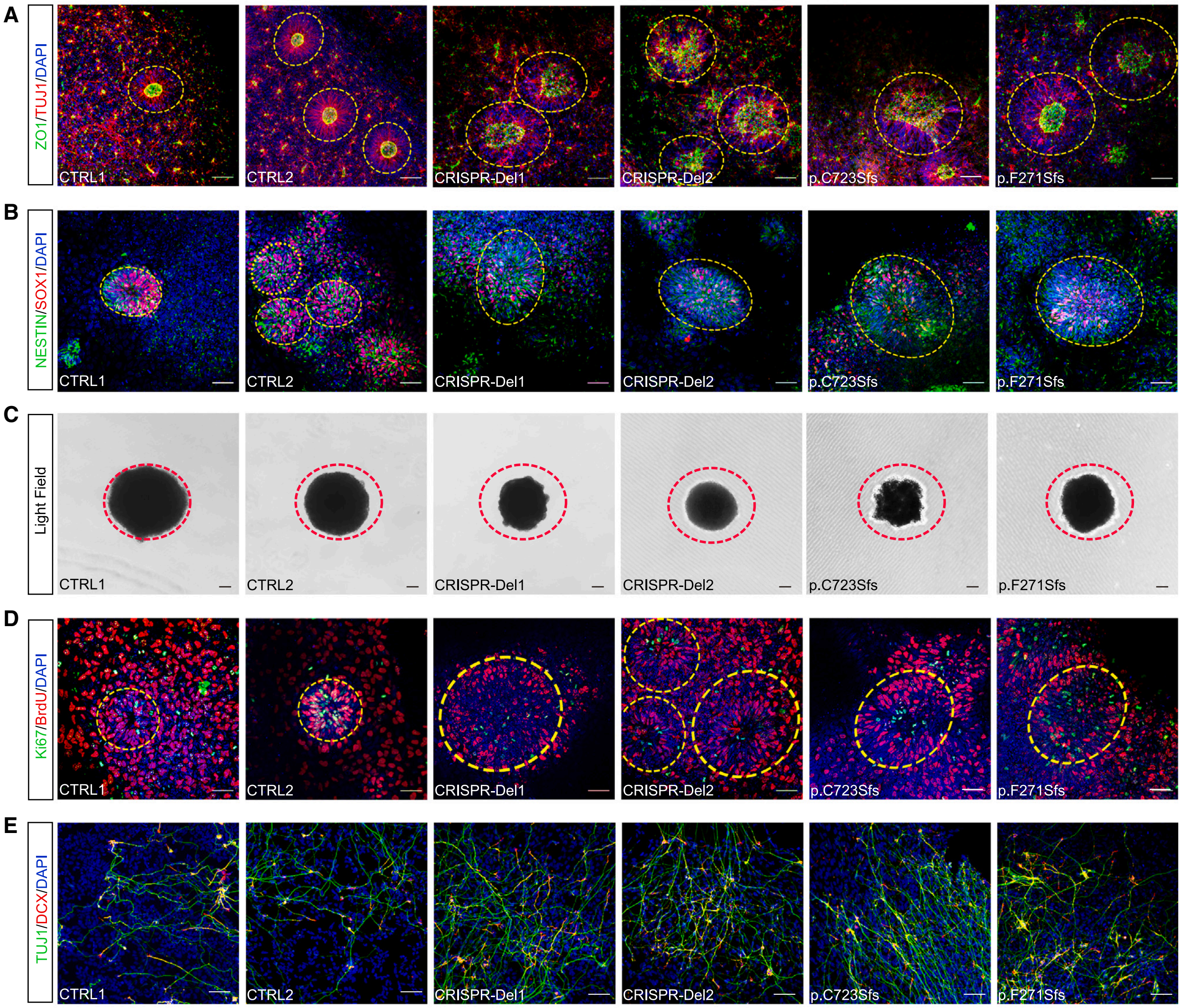

Figure 3. *MARK2* variant leads to aberrant polarity in iPSC-derived neural rosettes and imbalanced proliferation and differentiation in iPSC-derived NPCs

(A) Representative immunofluorescence images of TUJ1 (red) and ZO1 (green) in different iPSC-derived neural rosettes on the 10th day after neural induction. CTRL1 and CTRL2, 2 independent healthy adults without *MARK2* variants; p.C723Sfs and p.F271Sfs, 2 affected individuals with LOF *MARK2* variants; CRISPR-Del1 and CRISPR-Del2, 2 isogenic *MARK2* deletions produced by the CRISPR-Cas9 editing technology.

(B) Representative immunofluorescence images of SOX1 (red) and NESTIN (green) in different iPSC-derived neural rosettes on the 5th day after neural induction.

(C) Representative images of different iPSC-derived neurospheres on the 5th day after neural induction.

(D) Representative immunofluorescence images of BrdU (red) and Ki67 (green) in different iPSC-derived neural rosettes on the 4th day after neural induction.

(E) Representative immunofluorescence images of DCX (red) and TUJ1 (green) in different iPSC-derived NPCs on the 13th day after neural induction. Scale bar = 50 μm. The quantification and statistical analysis were showed in Figure S3.

(Figures 3B and S3C). Both the size of neurosphere and number of activated NPCs indicated aberrant self-renewal of NPC pool following *MARK2* loss.

In the iPSC-derived NPC stage, we conducted BrdU incorporation assays and Ki67 staining to assess proliferation capability (Figure 3D). The results demonstrated that there were significantly fewer BrdU$^+$ cells (Figure S3E) and Ki67$^+$ cells (Figure S3F) in mutant or CRISPR-Del NPCs compared to CTRLs. While the proliferation and differentiation of NPCs maintain a dynamic balance, we also evaluated the differentiation efficiency of NPCs using 2 neural markers, TUJ1 and DCX (Figure 3E). DCX$^+$ cells (Figure S3G) and TUJ1$^+$ cells (Figure S3H) in mutant and CRISPR-Del NPCs also showed a significant increase compared to CTRLs. Together, these results suggested that *MARK2* loss led to aberrant polarity and dis-organization in neural rosettes, thereby suppressing proliferation but promoting differentiation in NPCs.

Mark2 loss leads to abnormal cortical partition, ASD-like behaviors, and impaired memory in mice

To recapitulate the cellular phenotypes of an affected proband's iPSC-derived rosettes, we generated $Mark2^{+/-}$ (HET) mice utilizing the CRISPR-Cas9 system (Figures S4A, S4B, and S4D) to mimic *Mark2* loss *in vivo*. Consistently, the BrdU incorporation assay of mouse cortical NPCs (mNPCs) at E18.5 revealed significantly decreased $BrdU^+$ cells but increased $TUJ1^+$ cells in HET mice compared with WT ones (Figures S4E, S4H, and S4I), indicating the imbalanced proliferation and differentiation in early cortical NPCs upon *Mark2* loss. Additionally, downregulated $SOX1^+$ cells were also observed in the cortices of HET mice (Figures S4E and S4G), indicating altered neural self-renewal upon *Mark2* loss. As CTIP2 is expressed primarily in layer V, and SATB2 is expressed primarily in layers II/III,[38] we compared the thickness and the density of $CTIP2^+$ cells and $SATB2^+$ cells in mouse cortex. Whole density of $CTIP2^+$ cells and $SATB2^+$ cell was significantly increased in HET mice, although whole cortical thickness was similar (Figures S4F, S4J, S4K, and S4L). Particularly, the ratio of $CTIP2^+$ cells and $SATB2^+$ cells in layers V and VI showed significant increase (Figures S4F, S4M, and S4N). These results indicated abnormal cortical formation and partition upon *Mark2* loss.

In order to determine whether adult $Mark2^{+/-}$ mice exhibit the features of ASD and other NDDs observed in affected individuals, we performed a series of behavioral tests for $Mark2^{+/-}$ mice. Although HET mice had lower body weights (Figures S4B and S4C), they showed normal exploratory and locomotor activity in the open field tests (Figure S5A), as the total distance traveled (Figure S5C) and average speed (Figure S5D) were not different between HET mice and WT mice. Subsequently, we performed the three-chamber test to evaluate whether the mice exhibited the deficits in sociability and preference for novelty observed in ASD individuals.[39] In the social approach test (Figures 4A and 4B), WT mice spent significantly less time in the empty cage than in the cage containing the novel mice, while HET mice spent similar amounts of times between 2 cages. In the social novelty test (Figures 4E and 4F), WT mice spent significantly less time with the familiar mice than with the novel mice. Conversely, HET mice spent similar amounts of time with the familiar and novel mice. These social behavior tests demonstrated that HET mice presented reduced social motivation and pursuit of novelty. The marble-burying test and grooming test were used to evaluate stereotyped behaviors of ASD in rodents. We found that HET mice buried more marbles (Figures 4C and 4D) and spent more time grooming (Figure 4K) than WT mice. Additionally, in the elevated plus maze test, which was used to assess anxiety-like behavior of ASD, HET mice spent less time in the open arms than WT mice (Figures 4H and 4I). Together, these data suggested that *Mark2* loss in mice led to specific social deficits, stereotyped behavior, and anxiety that recapitulated the features of ASD in individuals with *MARK2* variants.

As affected individuals in our cohort also showed intellectual disability/developmental delay and language problems, we further assessed learning and memory capacity using the Y-maze (Figure 4G), the Barnes maze (Figure 4L), and the Morris water maze (Figure 4O). The Y-maze is designed to assess spatial memory and executive function. We found that the percentage of correct alterations made by HET mice was significantly decreased compared with WT mice (Figure 4J), indicating that HET mice exhibited abnormal spatial working memory. The results of the Barnes maze test suggested memory impairment in HET mice, as they spent significantly more time visiting (Figure 4N, left) and entering (Figures 4M and 4N, right) the target hole compared with WT ones. In the Morris water maze test (Figure 4O), HET mice showed a significantly longer latency to find the platform (Figures 4P and 4Q, right) and spent less time in the platform region when the platform was moved (Figure 4Q, left). Interestingly, during the training sessions of the Barnes maze and Morris water maze tests, the latencies of the HET mice were not significantly longer than those of the WT mice, suggesting similar learning abilities between the 2 genotypes. Nonetheless, we tested the recognition memory of mice using the novel object recognition test (Figure S5B) and found that HET mice spent similar amounts of time interacting with the novel object as WT mice (Figure S5E). Combined, these results implied that loss of *Mark2* impaired spatial memory.

MARK2 loss disrupts early neurogenesis via the downregulation of WNT/β-catenin signaling pathway

To further identify the molecular pathway of the *MARK2* variant in early neurogenesis, we performed RNA-seq for iPSC-derived NPCs on the 12th day after neural induction (Figure S6A) to detect significant dysregulated genes (Figure S6B, adjusted $p < 0.05$, $\log_2^{\text{Fold change}} > 1.5$). GO enrichment analysis of differentially expressed genes (DEGs) revealed the biological functional change related to muscle development, ear development, neuro fate commitment/specification, axonogenesis, synapse development, or material transport with *MARK2* loss (Figure S6C). GO enrichment analysis of downregulated genes are significantly involved in neuronal development (Figure 5A), including CNS neuron differentiation (GO: 0021953), forebrain development (GO: 0030900), axonogenesis (GO: 0007409), axon development (GO: 0061564), pattern specification process (GO: 0007389), negative regulation of neuron differentiation (GO: 0045665), regulation of neuron differentiation (GO: 0045664), regionalization (GO: 000 3002), axon guidance (GO: 0007411), and neuron projection guidance (GO: 0097485). There are 4 downregulated genes, *WNT3A*, *ASCL1*, *HES5*, and *FEZF2*, involved in all these GO terms, especially the terms related to early neuronal development, and *WNT3A* is the top decreased gene (Figure 5B). GSEA using up-/downregulated genes also revealed significant inhibition of the WNT signaling pathway in mutant cells (Figures 5C and S6D). Besides WNT3A, other

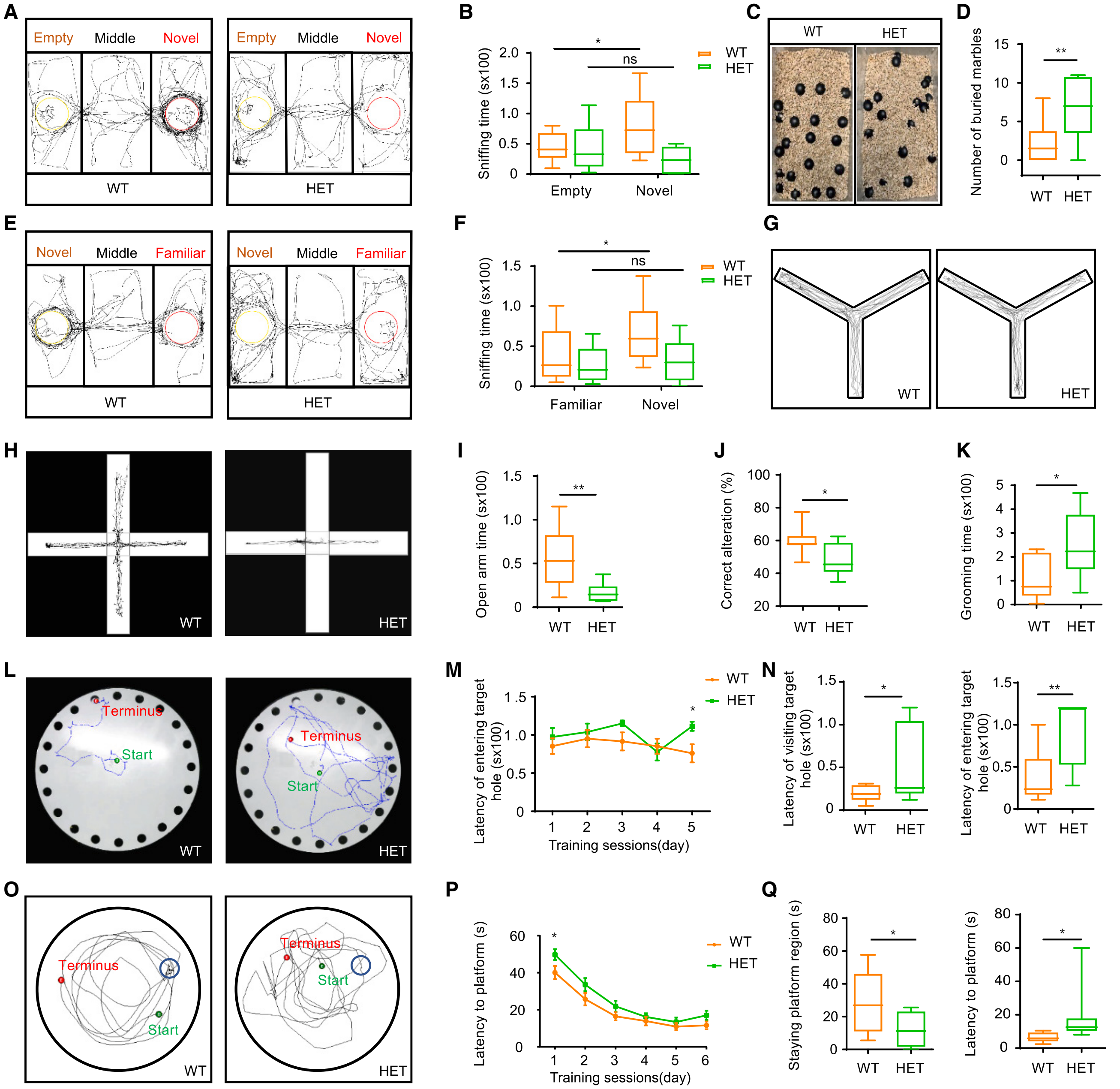

Figure 4. *Mark2* loss in mice leads to ASD-like behavior and impaired memory

(A and E) Trajectories of *Mark2* $^{+/+}$ (WT) and *Mark2* $^{+/-}$ (HET) mice in the three-chamber test (A, empty or novel; E, familiar or novel).

(B and F) Quantification analysis of sniffing time in the three-chamber test (B, empty or novel; F, familiar or novel).

(C, D, and K) Trajectories of WT and HET mice in the marble-burying test (C) and quantification analysis of the buried marbles (D) and grooming time (K).

(H and I) Trajectories of WT and HET mice in the elevated plus maze test (H) and quantification analysis of time spent in the open arms (I).

(G and J) Trajectories of WT and HET mice in the Y-maze test (G) and quantification analysis of the correct alternation (J).

(L–N) Trajectories of WT and HET mice in the Barnes maze test (L), quantification analysis of the latency of entering the target hole during the training sessions (M), and the latency of visiting target hole and of entering target hole during the test session (N).

(O–Q) Trajectories of WT and HET mice in the Morris water maze test (O), quantification analysis of the latency to find the platform during the training sessions (P), and the latency to finding the platform and staying platform quadrant during the test session (Q). WT = 9, HET = 9. The data were analyzed by Student's t test; *$p < 0.05$ and **$p < 0.01$.

key molecules of WNT signal (*WNT4*, *WNT7A*, *WNT7B*, *WNT8B*, *WNT10B*) were also significantly downregulated (Figure S6E). Furthermore, significantly decreased WNT3A protein was validated for mutant and CRISPR-Del cells (Figures 5D and 5F) along with decreased β-catenin (Figures 5D and 5E). A previous study showed that WNT3A, as a critical ligand, plays an important role in the activation of the WNT signaling pathway and is essential

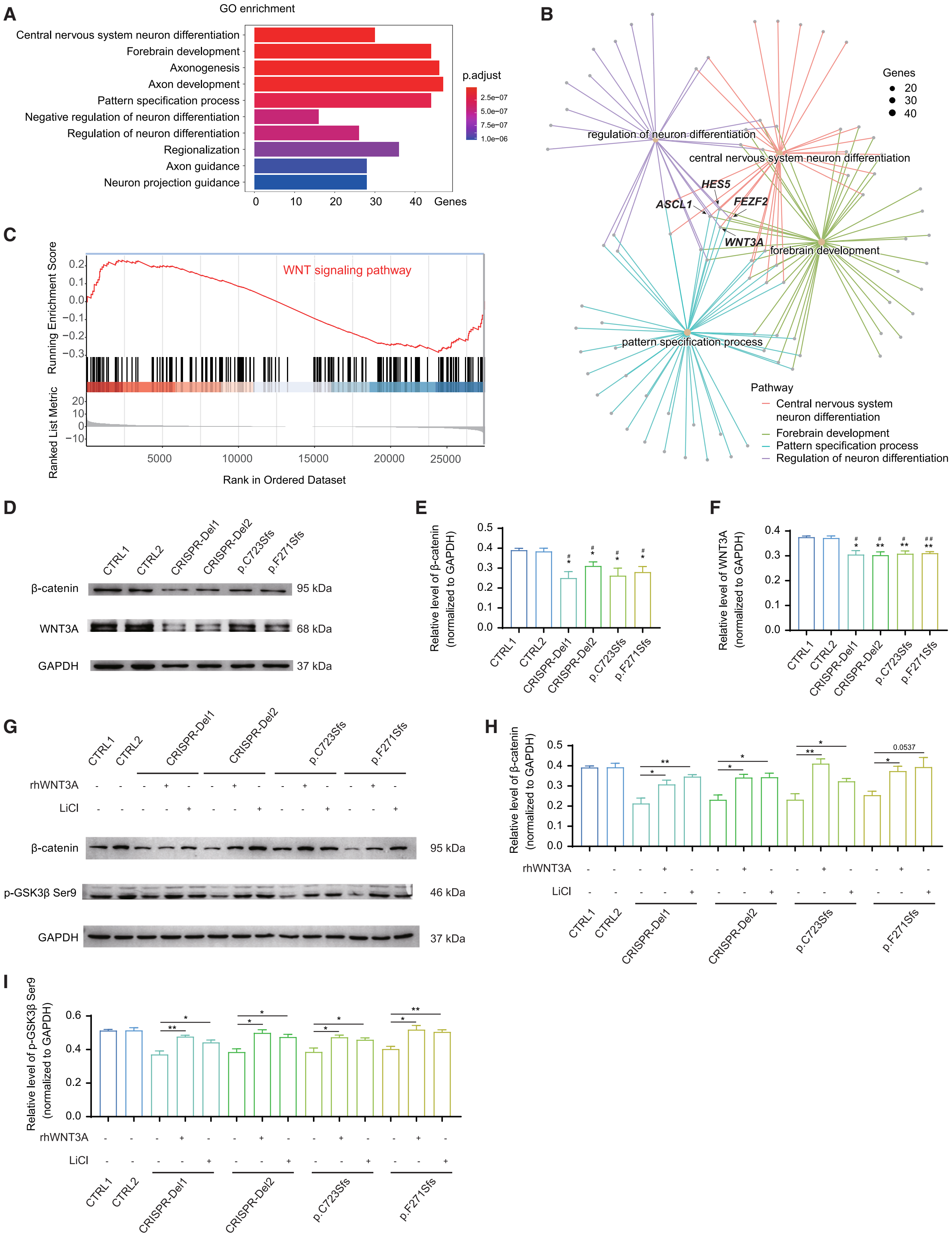

Figure 5. iPSC-derived NPCs revealed decreased WNT signaling pathway due to *MARK2* loss

(A) Gene Ontology (GO) analysis of differentially expressed genes (DEGs) between mutant iPSC-derived NPCs and CTRL ones show that the downregulated genes are enriched in multiple pathways related to early neuronal development.

(B) GO pathway network analysis showed the association of *WNT3A* with neuronal development, including neuron fate specification, forebrain development, central nervous system neuron differentiation, axonogenesis, and axon development. Size means number of genes involved in the specific pathway.

(C) The enrichment score and rank of the WNT/β-catenin signaling pathway from DEGs.

(legend continued on next page)

for the proliferation and differentiation of NPCs.[40] Hence, we hypothesized that *MARK2* loss led to abnormal early neuronal development via inhibition of the WNT signaling pathway.

In order to confirm the relationship between WNT signal pathway inhibition and *MARK2* loss, we treated mutant iPSC-NPCs with 100 ng/mL rhWNT3A. We found that rhWNT3A significantly increased the accumulation of *p*-GSK3β Ser9 (Figures 5G and 5I) and the accumulation of β-catenin in mutant iPSC-NPCs (Figures 5G and 5H). The rescue effect of rhWNT3A confirmed that *MARK2* loss results in relative inactivation of the WNT signaling pathway.

Lithium reverses the molecular and cellular phenotypes of mutant iPSC-derived NPCs and abnormal cortical partition of HET mice by activating the WNT/β-catenin signaling pathway

Lithium is a known activator of the WNT/β-catenin signaling pathway[41,42] and is widely prescribed for many behavioral disorders, such as bipolar disorder and schizoaffective disorder,[43] which are closely associated with ASD. We added LiCl at 0.7 mM, a routinely prescribed dosage for individuals with bipolar disorder, to the culture medium of iPSC-derived NPCs.[43,44] On the 10th day after neural induction, the protein levels of β-catenin, *p*-GSK3β Ser9 in mutant NPCs were significantly increased following LiCl treatment as similar to rhWNT3A treatment, even reaching the levels of control NPCs (Figures 5G, 5H, and 5I), suggesting WNT3A and *p*-GSK3β Ser9 as the target molecule of lithium rescue.

Considering the molecular effect of LiCl on WNT/β-catenin signaling activation, we replicated the IF experiment described above for LiCl-treated or rhWNT3A-treated mutant and CRISPR-Del iPSC-derived NPCs. Innovatively, the rescue effect of LiCl on the morphology of mutant neural rosettes was quite obvious, with the diameter of the neural rosettes being significantly decreased (Figures 6A and S7A) and the number of rosettes being significantly increased (Figures 6A and S7B). Also, correct localization of ZO1 and normal self-organization of TUJ1$^+$ cells were seen in mutant neural rosettes with LiCl treatment (Figure 6A). Moreover, the numbers of BrdU$^+$ (Figures 6B and S7C) and Ki67$^+$ cells (Figures 6B and S7D) in mutant and CRISPR-Del NPCs were significantly increased, almost reaching those of control NPCs or rhWNT3A treatment. We further compared the differentiation efficiencies of mutant NPCs before and after LiCl or rhWNT3A treatment. The numbers of TUJ1$^+$ (Figures 6C and S7F) and DCX$^+$ cells (Figures 6C and S7E) were significantly decreased after LiCl treatment. Both molecular and cellular phenotypes revealed that lithium rescues the abnormal developmental trajectories of *MARK2* loss via stimulation of the WNT signaling pathway.

To investigate the rescue effect of LiCl on cortical layer formation and partition in *Mark2*$^{+/-}$ mice, we treated pregnant female mice with 4.5 mg/L LiCl from E0.5 to E17.5 and analyzed proliferation and differentiation efficiency in the cortex at E18.5. We found that the number of BrdU$^+$ cells (Figures S8A and S8C) was significantly increased in HET mice treated with LiCl, but the number of TUJ1$^+$ cells was significantly decreased (Figures S8A and S8E). An obvious increase in the number of SOX1$^+$ cells was also observed in LiCl-treated HET mice compared with untreated HET mice (Figures S8A and S8D). These data demonstrated the rescue effects of lithium on the proliferation and activation of NPCs in mice with *Mark2* loss. We further compared the thickness of the cortical layers in HET mice before and after LiCl treatment using CTIP2 and SATB2 as markers of different cortex layers (Figure S8B). The results showed that LiCl treatment significantly rescued the abnormal formation of the mouse cortex, as the density of the CTIP2$^+$ and SATB2$^+$ cell in whole cortex (Figures S8F and S8G) and in specific cortical layers (Figures S8F and S8G) was similar between LiCl-treated HET and WT mice. These results were consistent with the rescue effects observed in Mut iPSC-derived NPCs.

Together, these *in vitro* and *in vivo* results demonstrated that pharmacological reactivation of the WNT/β-catenin signaling pathway by lithium can rescue aberrant cellular phenotypes in NPC with *MARK2* loss, thereby supporting a potential molecular link between *MARK2* loss and WNT/β-catenin signaling.

Discussion

In our study, we collected a multi-institutional global cohort of 31 individuals with clinically relevant *MARK2* variants and presented comprehensive clinical features and variant profiles of *MARK2*-associated ASD. Affected individuals frequently exhibit typical facial features (65%), including a prominent forehead, a broad nasal root, and larger or dysplastic ears in addition to vision problems; male genitourinary involvement and occasional skeletal involvement implying that *MARK2*-associated ASD frequently presents with other physical and morphologic comorbidities. Eighty percent of *MARK2* variants are LoF variants, supporting the idea that *MARK2* loss contributes to the development of ASD, as initially suggested from 2 large sequencing studies.[18,45]

(D–F) Representative western blot images (D) and quantification analysis of β-catenin (E) and WNT3A (F) accumulation in mutant and CRISPR-Del iPSC-derived NPCs compared with CTRLs.
(G–I) Representative western blot images (G) and quantification analysis of β-catenin (H) and *p*-GSK3β-Ser9 (I) accumulation in mutant, CRISPR-Del iPSC-derived NPCs with/without rhWNT3A (100 ng/mL) or LiCI treatment (0.7 mM). The data of at least 3 independent experiments were analyzed by Student's t test; $^*p < 0.05$ and $^{**}p < 0.01$(compared with CTRL1); $^{\#}p < 0.05$ and $^{\#\#}p < 0.01$ (compared with CTRL2).

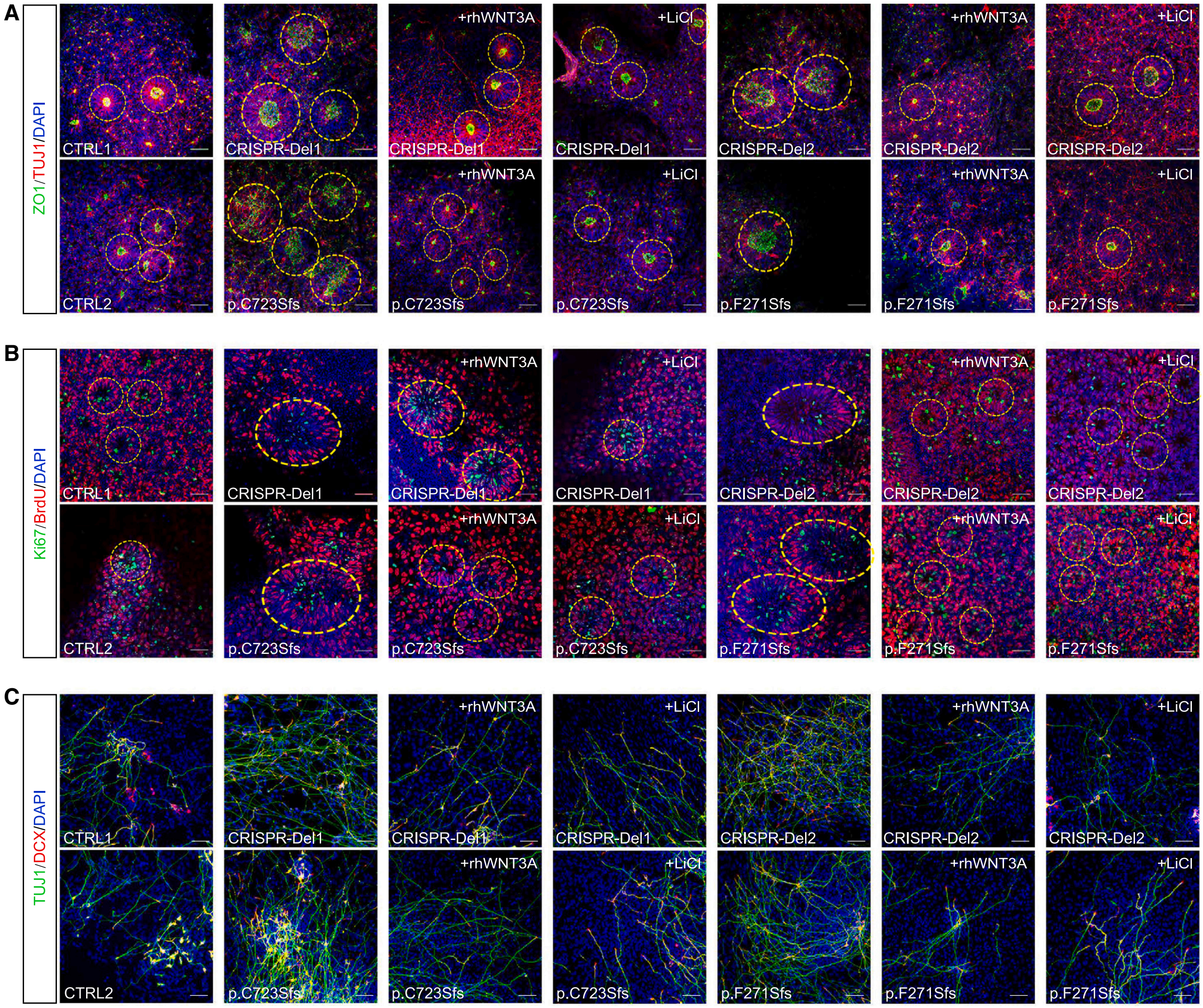

Figure 6. Lithium reverses the imbalance in the proliferation and differentiation of *MARK2* mutant iPSC-derived NPCs by activating the WNT/β-catenin signaling pathway

(A) Representative immunofluorescence images of ZO1 (green) and TUJ1 (red) in different iPSC-derived neural rosettes. CTRL1 and CTRL2, 2 independent healthy adults without *MARK2* variant; p.C723Sfs and p.F271Sfs, 2 affected individuals with LOF *MARK2* variants; and CRISPR-Del1 and CRISPR-Del2, 2 isogenic *MARK2* deletions produced by the CRISPR-Cas9 editing technology. Both CRISPR-Del and mutant iPSC-derived neural rosettes were treated with LiCl (0.7 mM) or rhWNT3A (100 ng/mL).

(B) Representative immunofluorescence images of Ki67 (green) and BrdU (red) in different iPSC-derived NPCs.

(C) Representative immunofluorescence images of TUJ1 (green) and DCX (red) in different iPSC-derived NPCs. Scale bar = 50 μm. The quantification and statistical analysis were showed in Figure S7.

We also observed high frequency of neurological comorbidities including intellectual disability/developmental delay (100%), speech-language problems (100%), and motor delay (62%). The IQ scores of 7 ASD individuals with LoF variants of *MARK2* from Zhou et al. reported were averagely 65.2, similar to that of ASD individuals with *CHD8/SHANK3* variants.[18] In addition, 1 individual in our cohort (P8) had not met ASD criteria until her last interview, although she presented with mixed receptive-expressive language disorder (personal communication), implying that *MARK2* is the candidate gene of NDDs, as previously reported.[45] Besides *MARK2*, another polarity gene of the *MARK* family, *MARK1*, has been recognized as a susceptibility gene for autism.[46] Our study also expanded polarity-related genes in ASD etiology.

MARK2 contains 5 domains, each with distinct functions necessary for its normal activity.[10] Previous studies have reported that *MARK2* mutants lacking the kinase domain led to neuronal polarity abrogation in hippocampal neurons.[12] Furthermore, mutations in the activating loop of the kinase domain, p.Thr208Ala and p.Ser212Ala, result in abnormal differentiation and neurite extension in neuroblastoma cells,[16] suggesting the critical role of the kinase domain in neuronal development. The KA1 domain, locating in the C terminus of MARK2, is conserved from yeast to humans and exerts an autoinhibitory effect on the kinase activity of MARK2 by blocking peptide substrate binding to the N and C lobes of the kinase domain.[11] Pathogenic variants in the KA1 domain impair this autoinhibition of MARK/PAR1 kinase activity.[33] We identified 4 variants in the ATP-binding pocket or the activation loop of kinase domain and 2 variants in the autoregulatory position of KA1 domain. Using integrative bioinformatics approaches, we predicted that these variants destabilize the interaction between these 2 domains and lead to loss of the autoregulation of MARK2. Further, our *in vitro*-transfected cell model confirmed that missense variants result in decreased *MARK2* expression comparable to LoF variants. Additionally, the phenotype associated with the missense variants was not significantly different from that of LoF variants. These data suggest that the missense variants impair the kinase or autoinhibitory activity of MARK2 following protein destabilization, resulting in similar cellular and molecular consequences as *MARK2* loss.

Multiple neurodevelopmental processes, including proliferation/neurogenesis, migration, neurite outgrowth, morphogenesis of dendrites and dendritic spines, and synaptogenesis and gliogenesis, have been reported to be altered in ASD.[47–50] Protein-protein interaction (PPI) networks of ASD-associated genes also confirmed the convergent pathways underlying ASD, including synaptic development, mitochondrial or metabolic processes, and WNT and MAPK signaling.[51–53] In order to explore the pathophysiological mechanism of *MARK2* loss underlying ASD, we generated mutant human iPSCs and described the cellular phenotypes of mutant neurons at early neural development such as fewer depolarized neural rosettes, smaller neurosphere formation, imbalanced proliferation, and differentiation in NPCs, which were similar to previous iPSC studies from other classic ASDs like fragile X syndrome (MIM: 300624), Rett syndrome (MIM: 312750), and *SHANK3* deletion.[48–50] Our results suggested that abnormal polarity and proliferation in mutant NPCs is a prerequisite for aberrant brain function in individuals with ASD. Furthermore, we have identified deficits in spatial learning, memory, and social preference among the *Mark2*$^{+/-}$ mice. Impaired spatial learning and memory have been previously documented in *Mark2*$^{+/-}$ mice.[54,55] Besides impaired social behavior, Caiola et al. reported decreased anxiety-like behavior in the plus maze and increased seizure susceptibility.[55] Although we didn't study seizure phenotypes in knockout mice, a high frequency of seizures/epilepsy (46.6%) was reported in our cohort.

The WNT signaling pathway mediates neurogenesis via several biological functions, including self-renewal, proliferation, and differentiation.[40,56–59] For example, WNT3A and WNT7A are indispensable for maintaining self-renewal and stimulating the proliferation of neural stem cells,[56,57] and WNT3A also plays a critical role in neural fate commitment.[56] The regulatory role of β-catenin signaling in the balance between cell proliferation and differentiation in the spinal cord has also been reported.[60] Abnormal WNT signaling pathway activity has been reported in mouse models or patient-derived iPSCs carrying mutations in other high-confidence ASD-associated genes, such as *SHANK3* and *TBR1* (MIM: 604616).[42,61] The transcriptomic profiling of our mutant iPSC-derived NPCs revealed a reduced WNT/β-catenin signaling pathway, reasonably explaining imbalanced proliferation and differentiation in mutant NPCs. Decreased WNT3A and SOX1, and aberrant self-renewal, was seen in mutant neural rosettes, and developmental phenotypes in mutant NPCs were consistent with that of *WNT3A/WNT7A* depletion.[56,57,59,60,62] Furthermore, abnormal phenotypes of mutant iPSC-derived NPCs were completely reversed *in vitro* by treatment with exogenous rhWNT3A. Our study associated the WNT/β-catenin signaling pathway with *MARK2*-related ASD.

To date, several genes encoding members in the WNT/β-catenin signaling pathway, including *PTEN* (MIM: 608309), *ADNP* (MIM: 611386), *ARID1B* (MIM: 614556), *CHD8* (MIM: 610528),[5,6,53,63] the activator of β-catenin signaling *CTNNB1* (MIM: 116806),[64] and *WNT1* (MIM: 164820),[65] have been associated with ASD with high confidence. β-catenin, as a highly conserved armadillo repeat protein family member, is encoded by *CTNNB1*, and LoF variants of *CTNNB1* cause a broad ASD phenotype.[64,66] We compared the clinical features of 120 individuals with germline likely pathogenic/pathogenic *CTNNB1* variants[64] with those of the ASD individuals studied herein (Table S6). The top rank features of individuals with the *CTNNB1* variant are intellectual disability/developmental delay (94.1%), motor delay (93.7%), delayed speech and language development/ASD (90.4%), and mild/severe eye problems (87.5%). The phenotypic similarity between 2 different cohorts also suggested the molecular role of the WNT/β-catenin signaling pathway in *MARK2*-related ASD.

Lithium, as a mood stabilizer, has been routinely prescribed to treat bipolar disorder for decades.[43,44] Previous *in vitro* and *in vivo* studies have proven that lithium directly activates the WNT/β-catenin signaling pathway.[42,57,67–70] By activating the WNT/β-catenin signaling pathway, lithium promotes the proliferation of NPCs and improves behavioral performance in a mouse model of Down syndrome (MIM: 190685)[67] and spatial memory impairment and neurodegeneration in a mouse model of Alzheimer disease (MIM: 104300).[70] Lithium can also directly enhance the proliferation of hippocampal progenitors *in vitro* in a dose-dependent manner.[68] The ability of lithium to rescue spine and synaptic defects has been reported in conditional *Tbr1*$^{+/-}$ adult mice presenting ASD-like behaviors[42] and APP/PS1 mice presenting impaired learning and memory.[69] Siavash Fazel Darbandi generated ASD mice with conditional *Tbr1*^{layer6} knockout and found that both cellular and behavioral abnormalities, including immature dendritic spines reducing synaptic density and decreased social interactions between young mice, were rescued with LiCl treatment.[42] In this study, we administered the clinically used dosage of lithium[31,33] to mutant iPSCs and *Mark2*$^{+/-}$ (HET) mice. Abnormal cellular phenotypes in mutant NPCs, including alterations in the size of the neurosphere, rosette formation, and the proliferation and differentiation of NPCs, were reversed by lithium treatment. Considering that ASD is an early brain malformation, we fed a LiCl-treated diet to pregnant *Mark2*$^{+/-}$ mice and studied the proliferation and differentiation of cortical neurons in *Mark2*$^{+/-}$ mouse fetuses. Abnormal cortex layer formation was also reversed. However, it is important to clarify that LiCl treatment was not directly applied to the *Mark2*$^{+/-}$ mice themselves, and the rescue evidence is indirect. In the future, therapeutic roles of LiCl for affected individuals with *MARK2*-associated ASD, particularly for juveniles or adults, need further experimental confirmation.

Conclusion

Our studies deciphered the clinical features and variant spectrum of *MARK2*-related ASD. Using human iPSC-derived NPCs *in vitro* and *Mark2*$^{+/-}$ mice *in vivo*, we elucidated the cellular phenotypes and molecular mechanism of *MARK2* loss during early neuronal development, which are associated with downregulation of the WNT/β-catenin signaling pathway. Moreover, we observed that lithium can reverse cellular phenotype in mutant iPSC-NPCs and abnormal cortical partition development in *Mark2*$^{+/-}$ mice via activation of the WNT/β-catenin signaling pathway, providing a potential treatment for *MARK2*-related ASD.

Data and code availability

The WES data will not be made publicly available, as they contain private information, but are available from the corresponding author upon request. All variants have also been submitted to ClinVar (http://www.ncbi.nlm.nih.gov/clinvar/, SCV005081699-SCV005081726). The raw sequence data of RNA-seq reported in this paper have been deposited in the Genome Sequence Archive (Genomics, Proteomics & Bioinformatics 2021) in the National Genomics Data Center,[71] China National Center for Bioinformation/Beijing Institute of Genomics, and Chinese Academy of Sciences and are publicly accessible at https://ngdc.cncb.ac.cn/gsa-human with accession number GSA-Human: HRA003632. The code used in this study is available upon request.

Acknowledgments

We thank all the families who participated in this study. We also thank James F. Gusella for his valuable comments and suggestions, Brendan C. Lanpher, M.D., for his involvement in patient care, and Filippo Pinto e Vairo, M.D., Ph.D., for his assistance with IRB logistics and patient consent. This work was supported by grants from the National Key Research and Development Program of China (project 2021YFA1101402), the Strategic Priority Research Program of the Chinese Academy of Sciences (nos. XDA16010300/XDA16021400), and the Open Project Program of the State Key Laboratory of Stem Cell and Reproductive Biology. This study was also supported by grants from the National Science Foundation of China (82371868, 82271428, 31900690, 82201314, and 82471194), Beijing Natural Science Foundation (7202019), Beijing Finance Bureau (CIP2024-0040), and Guangxi Science and Technology Program Project (Guike AB17195011).

Author contributions

M.G., C.-M.L., and X.C. were responsible for conception and design. M.G., X.C., C.-M.L., J.L., and Y.L. contributed to manuscript writing, and M.V.M.B.W. and M.T.Z. helped in manuscript editing. X.C., Z.Q., M.V.M.B.W., J.L., and H.L. managed the analysis and interpretation of all clinical/genetic data. J.L. and H.L. performed the western blot and qPCR experiments for PBMCs and *in vitro* HEK 293T/HeLa transfection assay for the spicing and missense variants. M.G., Y.L., J.L., Q.L., and Chen L. performed the iPSC-related experiments. M.G., Y.L., and H.L. conducted the animal experiments. M.T.Z., N.H., N.R.D., and R.U. performed structural modeling. H.Z. helped in iPSC culture and neural differentiation and drug treatment for iPSCs and HET mice. M.G. analyzed and visualized the RNA-seq data. All authors approved the final manuscript.

The following partners conducted individual recruitment and clinical/genetic information and photo collection (listed in alphabetical order): A.S.A.C., B.C., B.P., B.R.S., B.K., Carrie L., C. Ren, C.Z., C.C., C. Rieubland , D.C.K., D.B., E.v.B., E.W.K., F.T.M.-T., H.S., H.O., H.X., J.L.M., J.Z., J.A.M.-R., J.G., J.P., K.L.v.G., K.P., L.E.K., L.E., M.-J.H.v.d.B., M.W., M.V.M.B.W., M.J.F., A.M.I., M.D.A., C.M., N.J.B., O.S., P.Z., P.B., R.H.v.J., S.D.M., S.E., S.M.H., S.S.H., T.W., V.W., W.F., W.-H.T., W.V.K., X.W., Y.Y., Y.S., Y.R., Z.Q., and L.R.

Declaration of interests

The authors declare no competing interests.

Supplemental information

Supplemental information can be found online at https://doi.org/10.1016/j.ajhg.2024.09.006.

Received: March 25, 2024
Accepted: September 25, 2024
Published: October 16, 2024

References

1. Lai, M.C., Lombardo, M.V., and Baron-Cohen, S. (2014). Autism. Lancet *383*, 896–910.
2. Zhou, H., Xu, X., Yan, W., Zou, X., Wu, L., Luo, X., Li, T., Huang, Y., Guan, H., Chen, X., et al. (2020). Prevalence of Autism Spectrum Disorder in China: A Nationwide Multi-center Population-based Study Among Children Aged 6 to 12 Years. Neurosci. Bull. *36*, 961–971.
3. Baio, J., Wiggins, L., Christensen, D.L., Maenner, M.J., Daniels, J., Warren, Z., Kurzius-Spencer, M., Zahorodny, W., Robinson Rosenberg, C., White, T., et al. (2018). Prevalence of Autism Spectrum Disorder Among Children Aged 8 Years - Autism and Developmental Disabilities Monitoring Network, 11 Sites, United States, 2014. MMWR. Surveill. Summ. *67*, 1–23.
4. Tammimies, K., Marshall, C.R., Walker, S., Kaur, G., Thiruvahindrapuram, B., Lionel, A.C., Yuen, R.K.C., Uddin, M.,

Roberts, W., Weksberg, R., et al. (2015). Molecular Diagnostic Yield of Chromosomal Microarray Analysis and Whole-Exome Sequencing in Children With Autism Spectrum Disorder. JAMA *314*, 895–903.

5. Schaaf, C.P., Betancur, C., Yuen, R.K.C., Parr, J.R., Skuse, D.H., Gallagher, L., Bernier, R.A., Buchanan, J.A., Buxbaum, J.D., Chen, C.A., et al. (2020). A framework for an evidence-based gene list relevant to autism spectrum disorder. Nat. Rev. Genet. *21*, 367–376.
6. Satterstrom, F.K., Kosmicki, J.A., Wang, J., Breen, M.S., De Rubeis, S., An, J.Y., Peng, M., Collins, R., Grove, J., Klei, L., et al. (2020). Large-Scale Exome Sequencing Study Implicates Both Developmental and Functional Changes in the Neurobiology of Autism. Cell *180*, 568–584.e23.
7. Ruzzo, E.K., Perez-Cano, L., Jung, J.Y., Wang, L.K., Kashef-Haghighi, D., Hartl, C., Singh, C., Xu, J., Hoekstra, J.N., Leventhal, O., et al. (2019). Inherited and De Novo Genetic Risk for Autism Impacts Shared Networks. Cell *178*, 850–866.e826.
8. Kosmicki, J.A., Samocha, K.E., Howrigan, D.P., Sanders, S.J., Slowikowski, K., Lek, M., Karczewski, K.J., Cutler, D.J., Devlin, B., Roeder, K., et al. (2017). Refining the role of de novo protein-truncating variants in neurodevelopmental disorders by using population reference samples. Nat. Genet. *49*, 504–510.
9. Fu, J.M., Satterstrom, F.K., Peng, M., Brand, H., Collins, R.L., Dong, S., Wamsley, B., Klei, L., Wang, L., Hao, S.P., et al. (2022). Rare coding variation provides insight into the genetic architecture and phenotypic context of autism. Nat. Genet. *54*, 1320–1331.
10. Drewes, G., Ebneth, A., Preuss, U., Mandelkow, E.M., and Mandelkow, E. (1997). MARK, a novel family of protein kinases that phosphorylate microtubule-associated proteins and trigger microtubule disruption. Cell *89*, 297–308.
11. Emptage, R.P., Lemmon, M.A., Ferguson, K.M., and Marmorstein, R. (2018). Structural Basis for MARK1 Kinase Autoinhibition by Its KA1 Domain. Structure *26*, 1137–1143.e3.
12. Chen, Y.M., Wang, Q.J., Hu, H.S., Yu, P.C., Zhu, J., Drewes, G., Piwnica-Worms, H., and Luo, Z.G. (2006). interme kinase 2 functions downstream of the PAR-3/PAR-6/atypical PKC complex in regulating hippocampal neuronal polarity. Proc. Natl. Acad. Sci. USA *103*, 8534–8539.
13. Terabayashi, T., Itoh, T.J., Yamaguchi, H., Yoshimura, Y., Funato, Y., Ohno, S., and Miki, H. (2007). Polarity-regulating kinase partitioning-defective 1/microtubule affinity-regulating kinase 2 negatively regulates development of dendrites on hippocampal neurons. J. Neurosci. *27*, 13098–13107.
14. Sapir, T., Shmueli, A., Levy, T., Timm, T., Elbaum, M., Mandelkow, E.M., and Reiner, O. (2008). Antagonistic effects of doublecortin and MARK2/Par-1 in the developing cerebral cortex. J. Neurosci. *28*, 13008–13013.
15. Sapir, T., Sapoznik, S., Levy, T., Finkelshtein, D., Shmueli, A., Timm, T., Mandelkow, E.M., and Reiner, O. (2008). Accurate balance of the polarity kinase MARK2/Par-1 is required for proper cortical neuronal migration. J. Neurosci. *28*, 5710–5720.
16. Biernat, J., Wu, Y.Z., Timm, T., Zheng-Fischhöfer, Q., Mandelkow, E., Meijer, L., and Mandelkow, E.M. (2002). Protein kinase MARK/PAR-1 is required for neurite outgrowth and establishment of neuronal polarity. Mol. Biol. Cell *13*, 4013–4028.
17. Yoshimura, Y., Terabayashi, T., and Miki, H. (2010). Par1b/MARK2 phosphorylates kinesin-like motor protein GAKIN/KIF13B to regulate axon formation. Mol. Cell Biol. *30*, 2206–2219.
18. Zhou, X., Feliciano, P., Shu, C., Wang, T., Astrovskaya, I., Hall, J.B., Obiajulu, J.U., Wright, J.R., Murali, S.C., Xu, S.X., et al. (2022). Integrating de novo and inherited variants in 42,607 autism cases identifies mutations in new moderate-risk genes. Nat. Genet. *54*, 1305–1319.
19. Sobreira, N., Schiettecatte, F., Valle, D., and Hamosh, A. (2015). GeneMatcher: a matching tool for connecting investigators with an interest in the same gene. Hum. Mutat. *36*, 928–930.
20. Richards, S., Aziz, N., Bale, S., Bick, D., Das, S., Gastier-Foster, J., Grody, W.W., Hegde, M., Lyon, E., Spector, E., et al. (2015). Standards and guidelines for the interpretation of sequence variants: a joint consensus recommendation of the American College of Medical Genetics and Genomics and the Association for Molecular Pathology. Genet. Med. *17*, 405–424.
21. Pejaver, V., Byrne, A.B., Feng, B.J., Pagel, K.A., Mooney, S.D., Karchin, R., O'Donnell-Luria, A., Harrison, S.M., Tavtigian, S.V., Greenblatt, M.S., et al. (2022). Calibration of computational tools for missense variant pathogenicity classification and ClinGen recommendations for PP3/BP4 criteria. Am. J. Hum. Genet. *109*, 2163–2177.
22. Abou Tayoun, A.N., Pesaran, T., DiStefano, M.T., Oza, A., Rehm, H.L., Biesecker, L.G., Harrison, S.M.; and ClinGen Sequence Variant Interpretation Working Group ClinGen SVI (2018). Recommendations for interpreting the loss of function PVS1 ACMG/AMP variant criterion. Hum. Mutat. *39*, 1517–1524.
23. Kallberg, M., Margaryan, G., Wang, S., Ma, J., and Xu, J. (2014). RaptorX server: a resource for template-based protein structure modeling. Methods Mol. Biol. *1137*, 17–27.
24. Panneerselvam, S., Marx, A., Mandelkow, E.M., and Mandelkow, E. (2006). Structure of the catalytic and ubiquitin-associated domains of the protein kinase MARK/Par-1. Structure *14*, 173–183.
25. Jumper, J., Evans, R., Pritzel, A., Green, T., Figurnov, M., Ronneberger, O., Tunyasuvunakool, K., Bates, R., Žídek, A., Potapenko, A., et al. (2021). Highly accurate protein structure prediction with AlphaFold. Nature *596*, 583–589.
26. Eswar, N., Webb, B., Marti-Renom, M.A., Madhusudhan, M.S., Eramian, D., Shen, M.Y., Pieper, U., and Sali, A. (2006). Comparative protein structure modeling using Modeller. Curr. Protoc. Bioinformatics *15*, Unit-5.6.
27. Van Durme, J., Delgado, J., Stricher, F., Serrano, L., Schymkowitz, J., and Rousseau, F. (2011). A graphical interface for the FoldX forcefield. Bioinformatics *27*, 1711–1712.
28. Dinkel, H., Michael, S., Weatheritt, R.J., Davey, N.E., Van Roey, K., Altenberg, B., Toedt, G., Uyar, B., Seiler, M., Budd, A., et al. (2012). ELM–the database of eukaryotic linear motifs. Nucleic Acids Res. *40*, D242–D251.
29. Liu, F., Liang, C., Li, Z., Zhao, S., Yuan, H., Yao, R., Qin, Z., Shangguan, S., Zhang, S., Zou, L.P., et al. (2023). Haplotype-specific MAPK3 expression in 16p11.2 deletion contributes to variable neurodevelopment. Brain *146*, 3347–3363.
30. Chen, C., Jiang, P., Xue, H., Peterson, S.E., Tran, H.T., McCann, A.E., Parast, M.M., Li, S., Pleasure, D.E., Laurent, L.C., et al. (2014). Role of astroglia in Down's syndrome revealed by patient-derived human-induced pluripotent stem cells. Nat. Commun. *5*, 4430.
31. Chen, S., Zhou, Y., Chen, Y., and Gu, J. (2018). fastp: an ultra-fast all-in-one FASTQ preprocessor. Bioinformatics *34*, i884–i890.

32. Wiel, L., Baakman, C., Gilissen, D., Veltman, J.A., Vriend, G., and Gilissen, C. (2019). MetaDome: Pathogenicity analysis of genetic variants through aggregation of homologous human protein domains. Hum. Mutat. *40*, 1030–1038.
33. Moravcevic, K., Mendrola, J.M., Schmitz, K.R., Wang, Y.H., Slochower, D., Janmey, P.A., and Lemmon, M.A. (2010). Kinase associated-1 domains drive MARK/PAR1 kinases to membrane targets by binding acidic phospholipids. Cell *143*, 966–977.
34. Zimmermann, M.T., Urrutia, R., Oliver, G.R., Blackburn, P.R., Cousin, M.A., Bozeck, N.J., and Klee, E.W. (2017). Molecular modeling and molecular dynamic simulation of the effects of variants in the TGFBR2 kinase domain as a paradigm for interpretation of variants obtained by next generation sequencing. PLoS One *12*, e0170822.
35. Elkabetz, Y., Panagiotakos, G., Al Shamy, G., Socci, N.D., Tabar, V., and Studer, L. (2008). Human ES cell-derived neural rosettes reveal a functionally distinct early neural stem cell stage. Genes Dev. *22*, 152–165.
36. Hribkova, H., Grabiec, M., Klemova, D., Slaninova, I., and Sun, Y.M. (2018). Calcium signaling mediates five types of cell morphological changes to form neural rosettes. J. Cell Sci. *131*, jcs206896.
37. Venere, M., Han, Y.G., Bell, R., Song, J.S., Alvarez-Buylla, A., and Blelloch, R. (2012). Sox1 marks an activated neural stem/progenitor cell in the hippocampus. Development *139*, 3938–3949.
38. Fame, R.M., MacDonald, J.L., and Macklis, J.D. (2011). Development, specification, and diversity of callosal projection neurons. Trends Neurosci. *34*, 41–50.
39. Cheng, Y., Wang, Z.M., Tan, W., Wang, X., Li, Y., Bai, B., Li, Y., Zhang, S.F., Yan, H.L., Chen, Z.L., et al. (2018). Partial loss of psychiatric risk gene Mir137 in mice causes repetitive behavior and impairs sociability and learning via increased Pde10a. Nat. Neurosci. *21*, 1689–1703.
40. Ciani, L., and Salinas, P.C. (2005). WNTs in the vertebrate nervous system: from patterning to neuronal connectivity. Nat. Rev. Neurosci. *6*, 351–362.
41. Lenox, R.H., and Wang, L. (2003). Molecular basis of lithium action: integration of lithium-responsive signaling and gene expression networks. Mol. Psychiatry *8*, 135–144.
42. Fazel Darbandi, S., Robinson Schwartz, S.E., Pai, E.L.L., Everitt, A., Turner, M.L., Cheyette, B.N.R., Willsey, A.J., State, M.W., Sohal, V.S., and Rubenstein, J.L.R. (2020). Enhancing WNT Signaling Restores Cortical Neuronal Spine Maturation and Synaptogenesis in Tbr1 Mutants. Cell Rep. *31*, 107495.
43. Miura, T., Noma, H., Furukawa, T.A., Mitsuyasu, H., Tanaka, S., Stockton, S., Salanti, G., Motomura, K., Shimano-Katsuki, S., Leucht, S., et al. (2014). Comparative efficacy and tolerability of pharmacological treatments in the maintenance treatment of bipolar disorder: a systematic review and network meta-analysis. Lancet Psychiatr. *1*, 351–359.
44. Fransson, F., Werneke, U., Harju, V., Öhlund, L., de Man Lapidoth, J., Jonsson, P.A., Stegmayr, B., Renberg, E.S., and Ott, M. (2022). Kidney function in patients with bipolar disorder with and without lithium treatment compared with the general population in northern Sweden: results from the LiSIE and MONICA cohorts. Lancet Psychiatr. *9*, 804–814.
45. Hamanaka, K., Miyake, N., Mizuguchi, T., Miyatake, S., Uchiyama, Y., Tsuchida, N., Sekiguchi, F., Mitsuhashi, S., Tsurusaki, Y., Nakashima, M., et al. (2022). Large-scale discovery of novel neurodevelopmental disorder-related genes through a unified analysis of single-nucleotide and copy number variants. Genome Med. *14*, 40.
46. Maussion, G., Carayol, J., Lepagnol-Bestel, A.M., Tores, F., Loe-Mie, Y., Milbreta, U., Rousseau, F., Fontaine, K., Renaud, J., Moalic, J.M., et al. (2008). Convergent evidence identifying MAP/microtubule affinity-regulating kinase 1 (MARK1) as a susceptibility gene for autism. Hum. Mol. Genet. *17*, 2541–2551.
47. Chiola, S., Edgar, N.U., and Shcheglovitov, A. (2022). iPSC toolbox for understanding and repairing disrupted brain circuits in autism. Mol. Psychiatry *27*, 249–258.
48. Kim, K.Y., Hysolli, E., and Park, I.H. (2011). Neuronal maturation defect in induced pluripotent stem cells from patients with Rett syndrome. Proc. Natl. Acad. Sci. USA *108*, 14169–14174.
49. Yi, F., Danko, T., Botelho, S.C., Patzke, C., Pak, C., Wernig, M., and Südhof, T.C. (2016). Autism-associated SHANK3 haploinsufficiency causes Ih channelopathy in human neurons. Science *352*, aaf2669.
50. Doers, M.E., Musser, M.T., Nichol, R., Berndt, E.R., Baker, M., Gomez, T.M., Zhang, S.C., Abbeduto, L., and Bhattacharyya, A. (2014). iPSC-derived forebrain neurons from FXS individuals show defects in initial neurite outgrowth. Stem Cells Dev. *23*, 1777–1787.
51. O'Roak, B.J., Vives, L., Girirajan, S., Karakoc, E., Krumm, N., Coe, B.P., Levy, R., Ko, A., Lee, C., Smith, J.D., et al. (2012). Sporadic autism exomes reveal a highly interconnected protein network of de novo mutations. Nature *485*, 246–250.
52. Arnett, A.B., Wang, T., Eichler, E.E., and Bernier, R.A. (2021). Reflections on the genetics-first approach to advancements in molecular genetic and neurobiological research on neurodevelopmental disorders. J. Neurodev. Disord. *13*, 24.
53. Iossifov, I., O'Roak, B.J., Sanders, S.J., Ronemus, M., Krumm, N., Levy, D., Stessman, H.A., Witherspoon, K.T., Vives, L., Patterson, K.E., et al. (2014). The contribution of de novo coding mutations to autism spectrum disorder. Nature *515*, 216–221.
54. Segu, L., Pascaud, A., Costet, P., Darmon, M., and Buhot, M.C. (2008). Impairment of spatial learning and memory in ELKL Motif Kinase1 (EMK1/MARK2) knockout mice. Neurobiol. Aging *29*, 231–240.
55. Caiola, H.O., Wu, Q., Soni, S., Wang, X.F., Monahan, K., Pang, Z.P., Wagner, G.C., and Zhang, H. (2023). Neuronal connectivity, behavioral, and transcriptional alterations associated with the loss of MARK2. Preprint at bioRxiv. https://doi.org/10.1101/2023.12.05.569759.
56. Lie, D.C., Colamarino, S.A., Song, H.J., Désiré, L., Mira, H., Consiglio, A., Lein, E.S., Jessberger, S., Lansford, H., Dearie, A.R., and Gage, F.H. (2005). Wnt signalling regulates adult hippocampal neurogenesis. Nature *437*, 1370–1375.
57. Qu, Q., Sun, G., Li, W., Yang, S., Ye, P., Zhao, C., Yu, R.T., Gage, F.H., Evans, R.M., and Shi, Y. (2010). Orphan nuclear receptor TLX activates Wnt/beta-catenin signalling to stimulate neural stem cell proliferation and self-renewal. Nat. Cell Biol. *12*, 31–40.
58. Rosso, S.B., Sussman, D., Wynshaw-Boris, A., and Salinas, P.C. (2005). Wnt signaling through Dishevelled, Rac and JNK regulates dendritic development. Nat. Neurosci. *8*, 34–42.
59. Ciani, L., Boyle, K.A., Dickins, E., Sahores, M., Anane, D., Lopes, D.M., Gibb, A.J., and Salinas, P.C. (2011). Wnt7a signaling promotes dendritic spine growth and synaptic strength through Ca(2)(+)/Calmodulin-dependent protein kinase II. Proc. Natl. Acad. Sci. USA *108*, 10732–10737.

60. Zechner, D., Fujita, Y., Hülsken, J., Müller, T., Walther, I., Taketo, M.M., Crenshaw, E.B., 3rd, Birchmeier, W., and Birchmeier, C. (2003). beta-Catenin signals regulate cell growth and the balance between progenitor cell expansion and differentiation in the nervous system. Dev. Biol. *258*, 406–418.
61. Qin, L., Ma, K., Wang, Z.J., Hu, Z., Matas, E., Wei, J., and Yan, Z. (2018). Social deficits in Shank3-deficient mouse models of autism are rescued by histone deacetylase (HDAC) inhibition. Nat. Neurosci. *21*, 564–575.
62. Hall, A.C., Lucas, F.R., and Salinas, P.C. (2000). Axonal remodeling and synaptic differentiation in the cerebellum is regulated by WNT-7a signaling. Cell *100*, 525–535.
63. Butler, M.G., Dasouki, M.J., Zhou, X.P., Talebizadeh, Z., Brown, M., Takahashi, T.N., Miles, J.H., Wang, C.H., Stratton, R., Pilarski, R., and Eng, C. (2005). Subset of individuals with autism spectrum disorders and extreme macrocephaly associated with germline PTEN tumour suppressor gene mutations. J. Med. Genet. *42*, 318–321.
64. Kayumi, S., Pérez-Jurado, L.A., Palomares, M., Rangu, S., Sheppard, S.E., Chung, W.K., Kruer, M.C., Kharbanda, M., Amor, D.J., McGillivray, G., et al. (2022). Genomic and phenotypic characterization of 404 individuals with neurodevelopmental disorders caused by CTNNB1 variants. Genet. Med. *24*, 2351–2366.
65. Martin, P.M., Yang, X., Robin, N., Lam, E., Rabinowitz, J.S., Erdman, C.A., Quinn, J., Weiss, L.A., Hamilton, S.P., Kwok, P.Y., et al. (2013). A rare WNT1 missense variant overrepresented in ASD leads to increased Wnt signal pathway activation. Transl. Psychiatry *3*, e301.
66. Butz, S., Stappert, J., Weissig, H., and Kemler, R. (1992). Plakoglobin and beta-catenin: distinct but closely related. Science *257*, 1142–1144.
67. Contestabile, A., Greco, B., Ghezzi, D., Tucci, V., Benfenati, F., and Gasparini, L. (2013). Lithium rescues synaptic plasticity and memory in Down syndrome mice. J. Clin. Invest. *123*, 348–361.
68. Wexler, E.M., Geschwind, D.H., and Palmer, T.D. (2008). Lithium regulates adult hippocampal progenitor development through canonical Wnt pathway activation. Mol. Psychiatry *13*, 285–292.
69. Xiang, J., Ran, L.Y., Zeng, X.X., He, W.W., Xu, Y., Cao, K., Dong, Y.T., Qi, X.L., Yu, W.F., Xiao, Y., and Guan, Z.Z. (2021). LiCl attenuates impaired learning and memory of APP/PS1 mice, which in mechanism involves alpha7 nAChRs and Wnt/beta-catenin pathway. J. Cell Mol. Med. *25*, 10698–10710.
70. Toledo, E.M., and Inestrosa, N.C. (2010). Activation of Wnt signaling by lithium and rosiglitazone reduced spatial memory impairment and neurodegeneration in brains of an APPswe/PSEN1DeltaE9 mouse model of Alzheimer's disease. Mol. Psychiatry *15*, 272–285.
71. CNCB-NGDC Members and Partners (2022). Database Resources of the National Genomics Data Center, China National Center for Bioinformation in 2022. Nucleic Acids Res. *50*, D27–D38.

The American Journal of Human Genetics, Volume *111*

Supplemental information

MARK2 variants cause autism spectrum disorder via the downregulation of WNT/β-catenin signaling pathway

Maolei Gong, Jiayi Li, Zailong Qin, Matheus Vernet Machado Bressan Wilke, Yijun Liu, Qian Li, Haoran Liu, Chen Liang, Joel A. Morales-Rosado, Ana S.A. Cohen, Susan S. Hughes, Bonnie R. Sullivan, Valerie Waddell, Marie-José H. van den Boogaard, Richard H. van Jaarsveld, Ellen van Binsbergen, Koen L. van Gassen, Tianyun Wang, Susan M. Hiatt, Michelle D. Amaral, Whitley V. Kelley, Jianbo Zhao, Weixing Feng, Changhong Ren, Yazhen Yu, Nicole J. Boczek, Matthew J. Ferber, Carrie Lahner, Sherr Elliott, Yiyan Ruan, Cyril Mignot, Boris Keren, Hua Xie, Xiaoyan Wang, Bernt Popp, Christiane Zweier, Juliette Piard, Christine Coubes, Frederic Tran Mau-Them, Hana Safraou, A. Micheil Innes, Julie Gauthier, Jacques L. Michaud, Daniel C. Koboldt, Odent Sylvie, Marjolaine Willems, Wen-Hann Tan, Benjamin Cogne, Claudine Rieubland, Dominique Braun, Scott Douglas McLean, Konrad Platzer, Pia Zacher, Henry Oppermann, Lucie Evenepoel, Pierre Blanc, Laïla El Khattabi, Neshatul Haque, Nikita R. Dsouza, Michael T. Zimmermann, Raul Urrutia, Eric W. Klee, Yiping Shen, Hongzhen Du, Leonard Rappaport, Chang-Mei Liu, and Xiaoli Chen

Supplementary Appendix

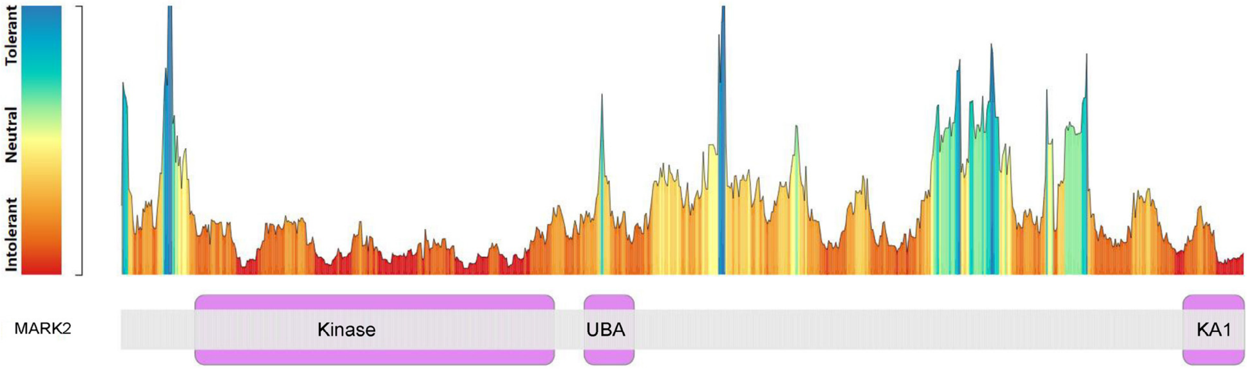

Figure S1. The missense variant tolerance landscape

Protein of MARK2 (GENCODE: ENST00000402010.2, RefSeq: NM_001039469.3, UniProt: Q7KZI7) was used. The ratios of missense over synonymous variant were calculated to indicate the regions that are intolerant to missense variation. The kinase and KA1 domain (purple parts) clearly show as intolerant compared with other parts.

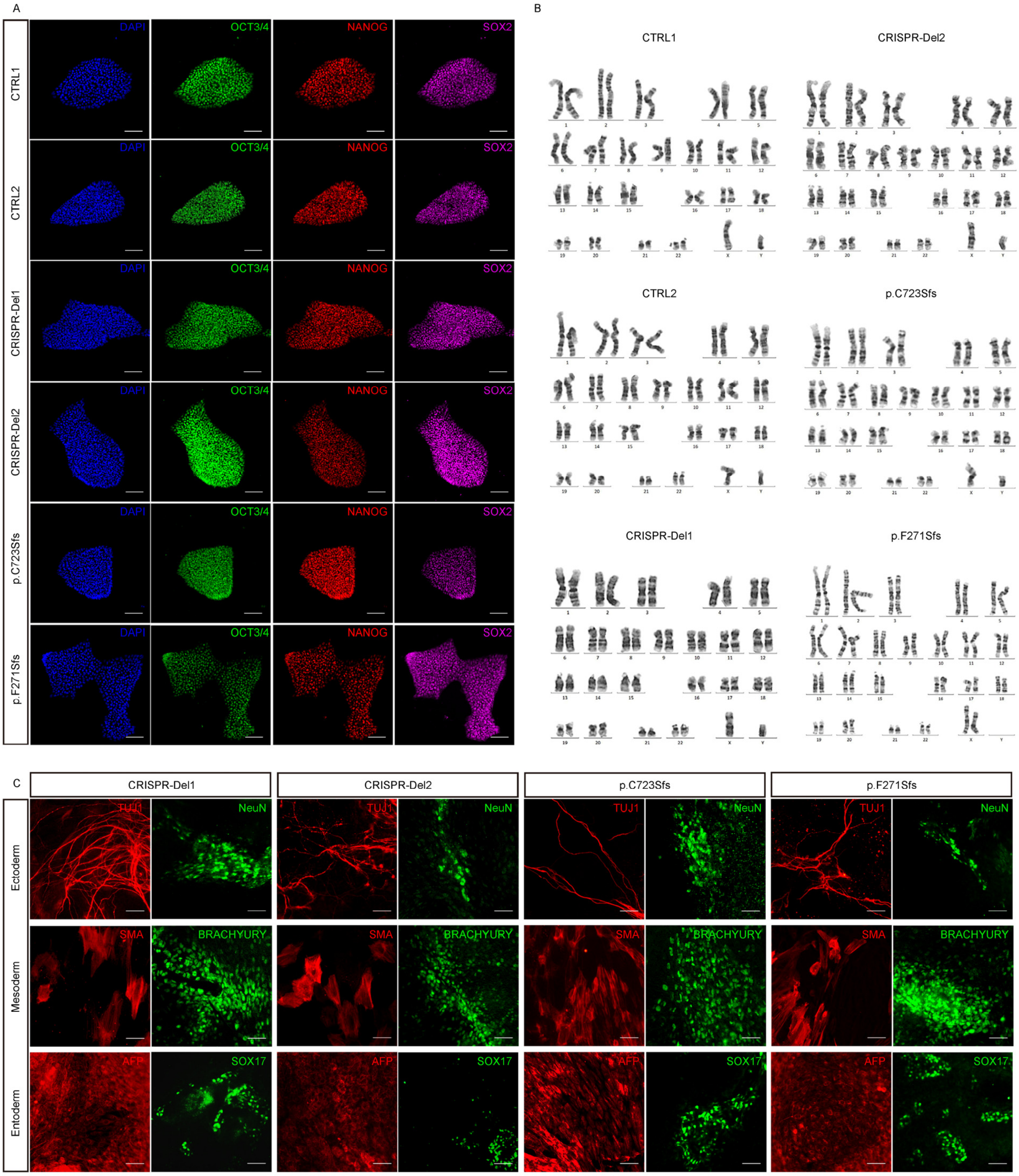

Figure S2. Representative validation images of iPSCs with different genotypes

A, Representative validation images of six iPSCs using several markers, OCT 3/4 (green), NANOG (red), and SOX2 (purple). Nuclei were stained with DAPI (blue). CTRL1 and CTRL2: two independent healthy adults without *MARK2* variant; p.C723Sfs and p.F271Sfs: two affected individuals with LoF *MARK2* variants; CRISPR-Del1 and CRISPR-Del2: two isogenic *MARK2* deletions produced by the CRISPR/Cas9 editing technology. scale bar = 50 μm. **B**, Representative karyotype images of six iPSCs separately. **C**, Representative images of differentiated iPSC EBs using a Human pluripotent stem cell identification kit. Differentiated iPSCs were fixed for immunocytology analysis for the ectoderm (TUJ1, NeuN), mesoderm (SMA, BRACHYURY) and entoderm (AFP, SOX17) lineages. scale bar = 50 μm.

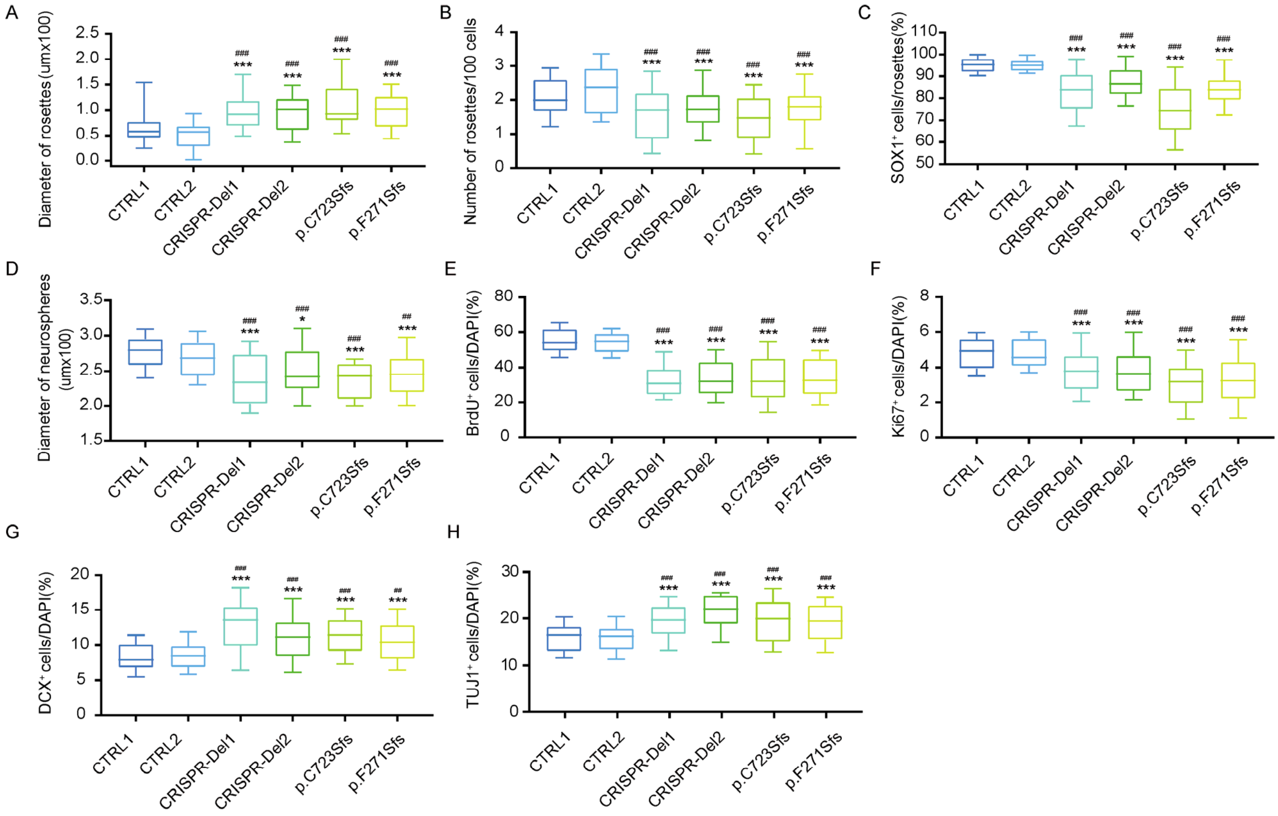

Figure S3. Quantification analysis of iPSC-derived neural rosettes and NPCs.

A-H the quantification analysis of rosette diameter (**A**, *n*=12 rosettes), rosette number (**B**) in **Fig 3A**, SOX1$^+$ cells (**C**) in **Fig 3B**, neurosphere diameter (**D**, *n*=12 neurospheres) in **Fig 3C**, BrdU$^+$ cells (**E**) and Ki67$^+$ cells (**F**) in **Fig 3D**, DCX$^+$ cells (**G**) and TUJ1$^+$ cells (**H**) in **Fig 3E**. The data of at least three independent experiments were analyzed by Student's t test; *p<0.05 and ***p<0.001(compared with CTRL1); $^{##}p$<0.01 and $^{###}p$<0.001(compared with CTRL2).

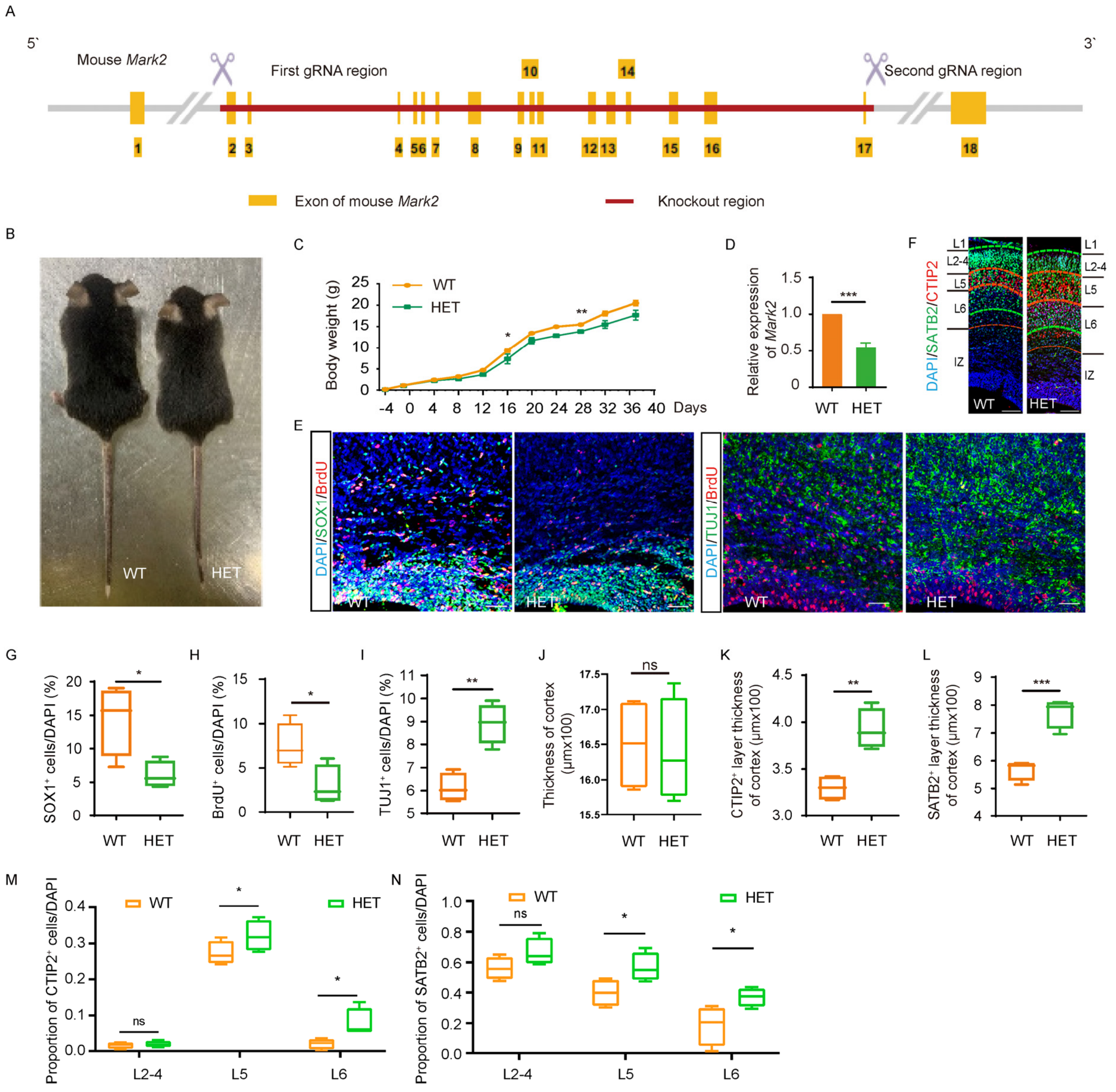

Figure S4. ***Mark2*** **loss in mice affects the proliferation and differentiation of NPCs** ***in vitro.***

A, Schematic of *Mark2* knockout mice. **B-C**, Body size (**B**) and growth curve (**C**) of *Mark2*$^{+/+}$ (WT) mice and *Mark2*$^{+/-}$ (HET) mice in 6 weeks. **D,** Expression of *Mark2* of HET and WT mice. Total RNAs were isolated from the cortex in E18.5 mice, and GAPDH was used as the internal parameter. **E-F**, Representative images of immunofluorescence staining for BrdU (red) and SOX1 (green), BrdU (red) and TUJ1 (green), CTIP2 (red) and SATB2 (green) in the cortical region above the subventricular zone (SVZ) in E18.5 mice, L1, L2-4, L5, L6 and IZ were marked to point out layers 1-6 and intermediate zone of mouse neocortex, the thick red dotted line were used to point out the CTIP2^{+} layer in L5, the thick green dotted line were used to point out the SATB2^{+} layer in L2-6, and the thin red dotted lines was used to point out the border of L6 with farthest CTIP2^{+}

cells located. **G-I**, Quantification analysis of SOX1$^+$ cells (**G**), BrdU$^+$ cells (**H**), TUJ1$^+$ cells (**I**), **J-L**. Quantification analysis for the thickness of mice cortex. Total thickness of mice cortex from SVZ to the pial surface (**J**), thickness of CTIP2$^+$ layer (**K,** thick red dotted line), and thickness of SATB2$^+$ layer (**L,** thick green dotted line). **M-N**, Quantification analysis for proportion of CTIP2$^+$ or SATB2$^+$ cells in specifical mouse neocortex. The proportion were analysis using the number of CTIP2$^+$ or SATB2$^+$ cells divided by the number of DAPI, proportion of CTIP2$^+$ cells (**M**), and proportion of SATB2$^+$ cells (**N**), *n*=4. The data of at least three independent experiments were analyzed by Student's t test; *$p<0.05$, **$p<0.01$ and ***$p<0.001$. scale bar = 50 μm.

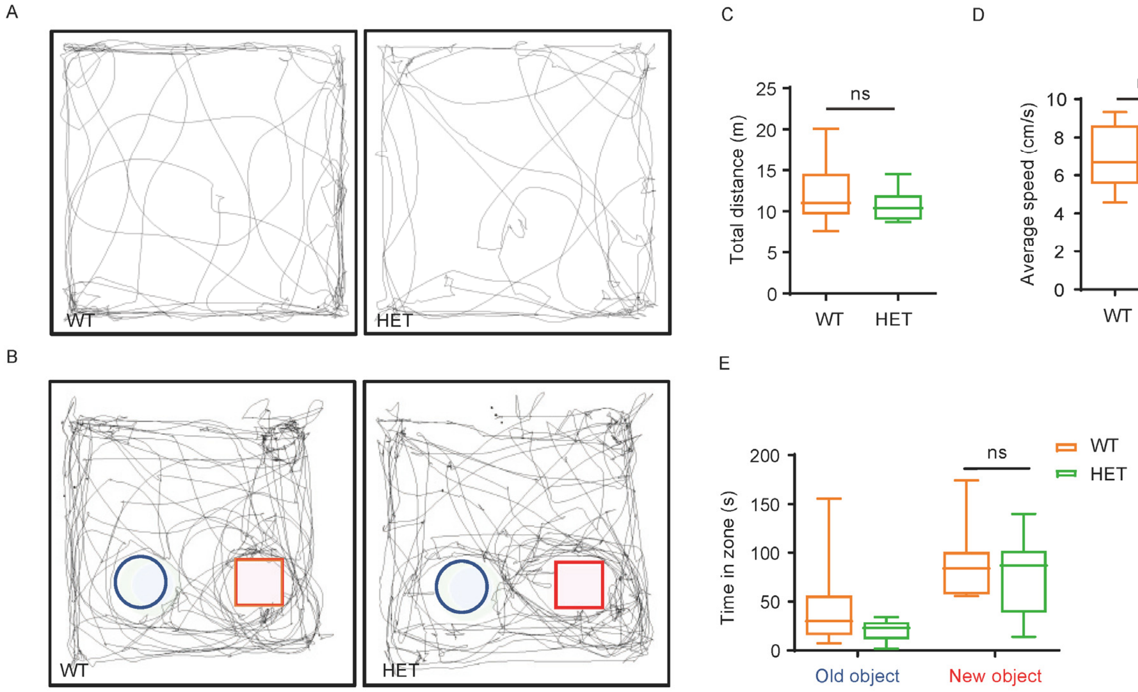

Figure S5. Open field and new object recognition tests in mice with *Mark2* loss

A-B, Trajectories of WT and HET mice in the open field test (**A**) and new object recognition test. (**B**). **C-D**, Quantification analysis of total distance (**C**) and average speed (**D**) between two genotypes in the open field test. **E**, Quantification analysis of time in zone in the new object recognition test (*n*=11). Time spend in contact with the object was used to represent for the new object recognition. The blue circle was used to point the location of the old object and red square was used to point the location of the new object. WT=11, HET=11. The data of at least three independent experiments were analyzed by Student's t test; ns: not significant.

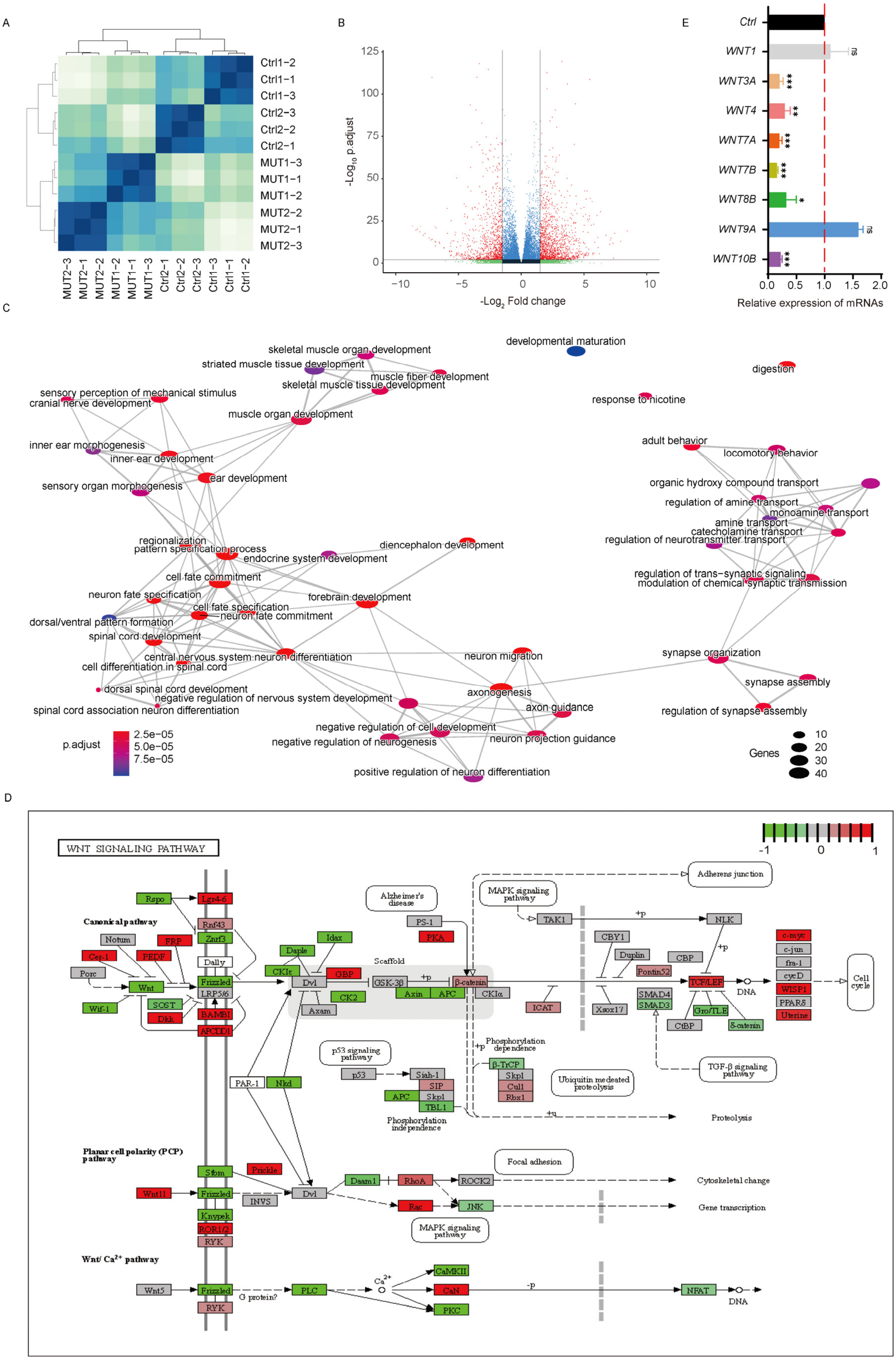
A
Ctrl1−2
Ctrl1−1
Ctrl1−3
Ctrl2−3
Ctrl2−2
Ctrl2−1
MUT1−3
MUT1−1
MUT1−2
MUT2−2
MUT2−1
MUT2−3
MUT2−3
MUT2−1
MUT2−2
MUT1−2
MUT1−1
MUT1−3
Ctrl2−1
Ctrl2−2
Ctrl2−3
Ctrl1−3
Ctrl1−1
Ctrl1−2
B
125
100
75
50
25
0
$-Log_{10}$ p.adjust
−10
−5
0
5
10
$-Log_2$ Fold change
E
Ctrl
WNT1
WNT3A
WNT4
WNT7A
WNT7B
WNT8B
WNT9A
WNT10B
ns
***
**
***
***
*
ns
***
0.0
0.5
1.0
1.5
2.0
Relative expression of mRNAs
C
skeletal muscle organ development
developmental maturation
striated muscle tissue development
muscle fiber development
digestion
skeletal muscle tissue development
sensory perception of mechanical stimulus
response to nicotine
cranial nerve development
muscle organ development
adult behavior
inner ear morphogenesis
locomotory behavior
inner ear development
ear development
organic hydroxy compound transport
sensory organ morphogenesis
regulation of amine transport
monoamine transport
amine transport
catecholamine transport
regionalization
regulation of neurotransmitter transport
pattern specification process
diencephalon development
endocrine system development
regulation of trans−synaptic signaling
cell fate commitment
modulation of chemical synaptic transmission
neuron fate specification
forebrain development
cell fate specification
neuron fate commitment
dorsal/ventral pattern formation
spinal cord development
central nervous system neuron differentiation
neuron migration
synapse organization
cell differentiation in spinal cord
dorsal spinal cord development
axonogenesis
synapse assembly
negative regulation of nervous system development
axon guidance
spinal cord association neuron differentiation
regulation of synapse assembly
negative regulation of cell development
negative regulation of neurogenesis
neuron projection guidance
positive regulation of neuron differentiation
p.adjust
2.5e−05
5.0e−05
7.5e−05
Genes
10
20
30
40
D
WNT SIGNALING PATHWAY
-1
0
1
Canonical pathway
Rspo
Lgr4-6
Rnf43
Znrf3
Notum
FRP
Cer-1
PEDF
Dally
Porc
Wnt
Frizzled
LRP5/6
Wif-1
SOST
Dkk
BAMBI
APCDD1
Daple
Idax
CKIε
GBP
Dvl
CK2
Axam
Alzheimer's disease
PS-1
PKA
Scaffold
GSK-3β
Axin
APC
+p
β-catenin
CKIα
ICAT
MAPK signaling pathway
TAK1
NLK
+p
CBY1
Duplin
CBP
Pontin52
SMAD4
SMAD3
Xsox17
TCF/LEF
Groucho/TLE
CtBP
β-catenin
DNA
Adherens junction
c-myc
c-jun
fra-1
cycD
WISP1
PPARδ
Uterine
Cell cycle
TGF-β signaling pathway
Phosphorylation dependence
β-TrCP
Skp1
Cul1
Rbx1
Ubiquitin mediated proteolysis
+u
Proteolysis
p53 signaling pathway
p53
Siah-1
SIP
APC
Skp1
TBL1
Phosphorylation independence
PAR-1
Nkd
Planar cell polarity (PCP) pathway
Stbm
Prickle
Wnt11
Frizzled
INVS
Knypek
ROR1/2
RYK
Dvl
Daam1
RhoA
ROCK2
Rac
JNK
Focal adhesion
Cytoskeletal change
Gene transcription
MAPK signaling pathway
Wnt/ Ca^{2+} pathway
Wnt5
Frizzled
RYK
G protein?
PLC
Ca^{2+}
CaMKII
CaN
PKC
-p
NFAT
DNA

Figure S6. RNA-Seq analyses of iPSC-derived NPCs.

A, Correlation heatmap of RNA-Seq of control (CTRL1) and mutant iPSC-derived NPCs (Mut: p.C723Sfs, *n*=3 experiment). **B**, Example volcano plot. Points on top-right and top-left corners are considered the most promising genes ($P<0.05$, $\log_2$Foldchange>1.5). **C**, Association network diagram between feature sets through GO analysis. All those feature sets of GO were enriched through downregulated genes (Log_2FoldChange<-1.5, *p* value>0.05) in mutant neurospheres. **D,** Pathview of WNT signaling pathway through GSEA analysis. Gene involved in WNT signaling pathway were showed in different colors, which the upregulated genes were marked with red, downregulated gene were labelled with green, and other genes were marked with gray. **E**, Decreased expression of several WNT genes (*WNT3A, WNT4, WNT7A, WNT7B, WNT8B, WNT10B*) in mutant hiPSC-derived NPCs were validated by quantitative RT-PCR. GAPDH was used as the internal reference and expressions were normalized by control iPSC-derived NPCs.

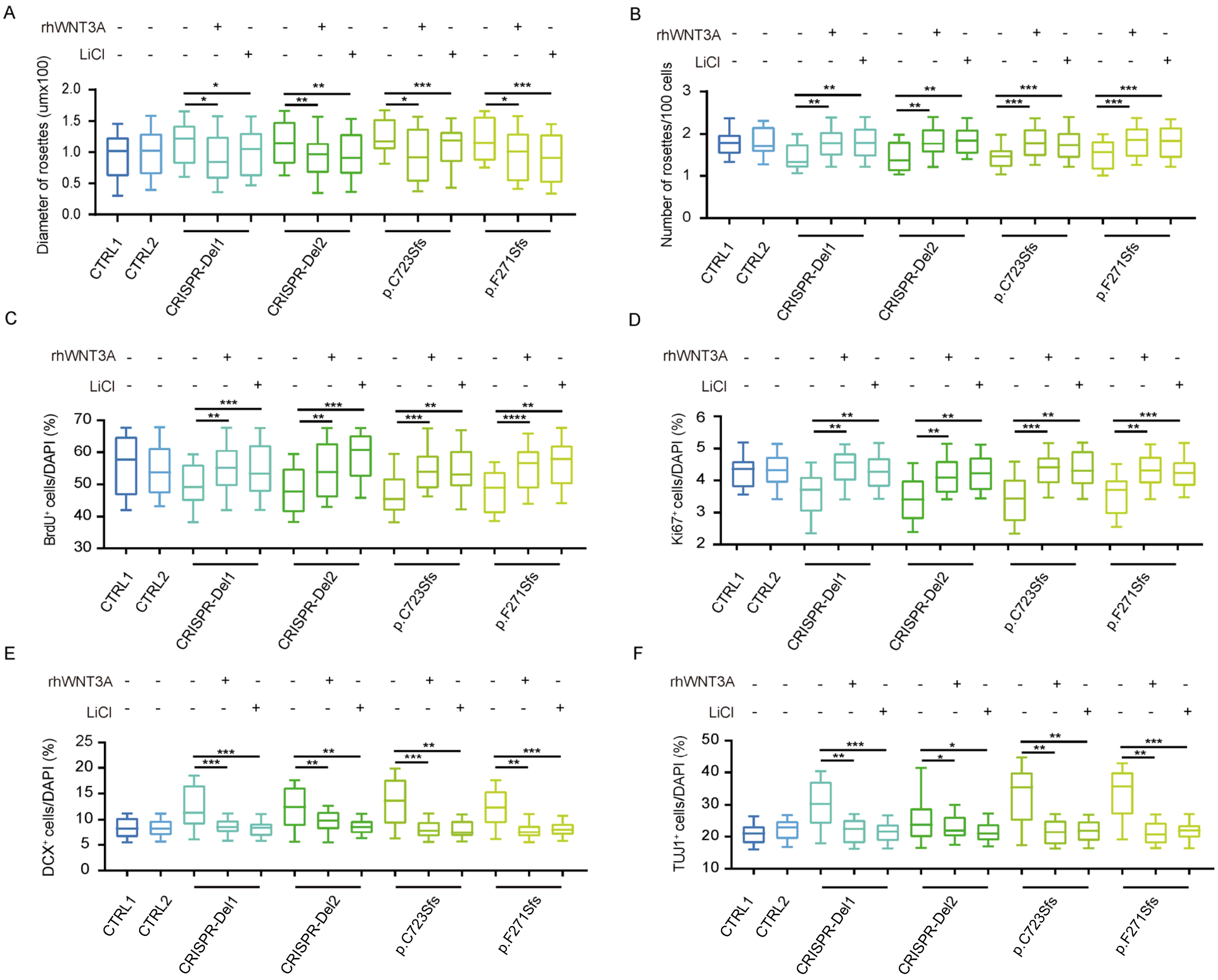

Figure S7. Quantification analysis of iPSC-derived neural rosettes and NPCs treated with LiCl or rhWNT3A.

A-F The quantification analysis of rosette diameter (**A**), rosettes number (**B**) in **Fig 6A**, BrdU$^+$ cells (**C**) and Ki67$^+$ cells (**D**) in **Fig 6B**, DCX$^+$ cells (**E**) and TUJ1$^+$ cells (**F**) in **Fig 6C**. The data of at least three independent experiments were analyzed by Student's t test; *$p<0.05$, **$p<0.01$ and ***$p<0.001$.

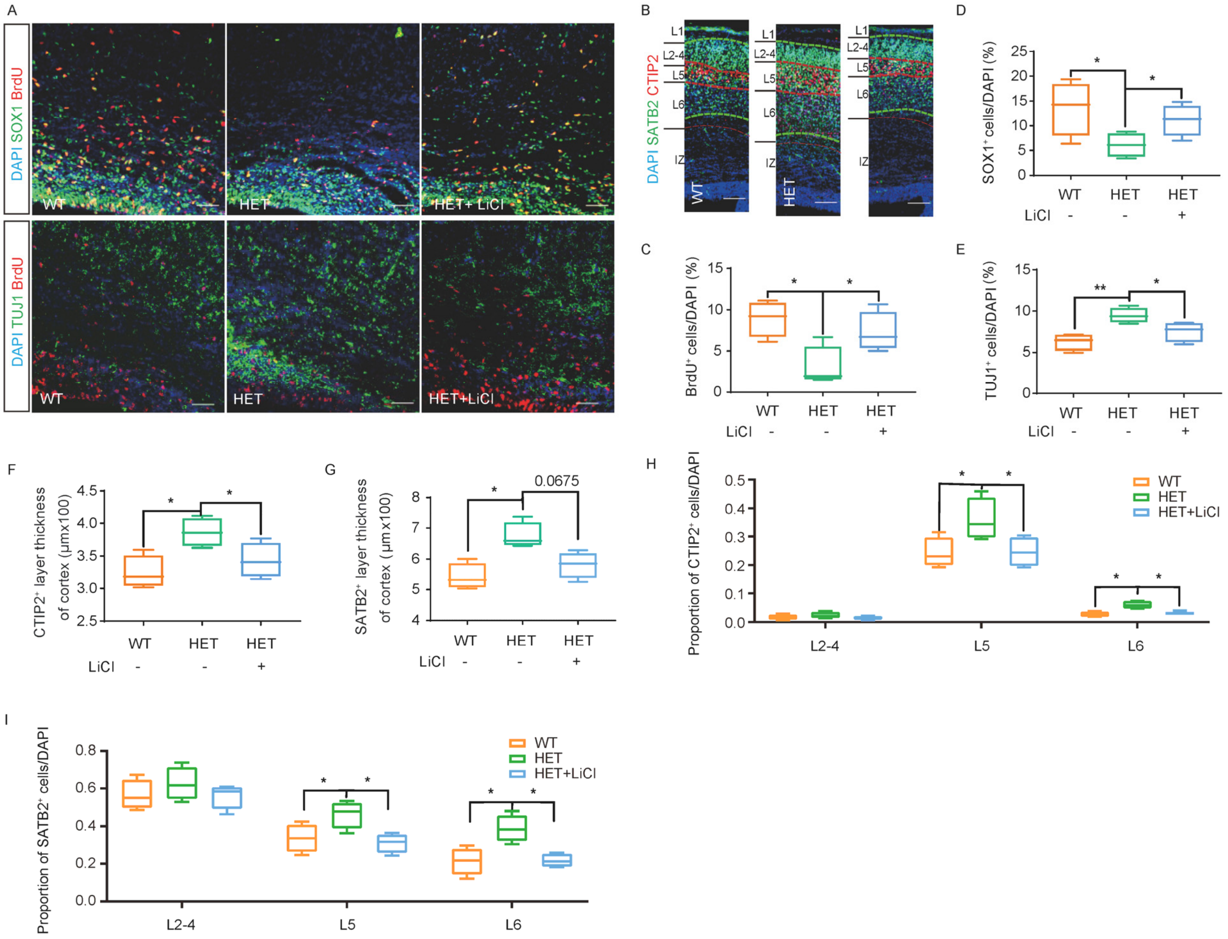

Figure S8. Abnormal cortical development in *Mark* $^{+/-}$ mice is rescued by LiCl

A-B, Representative images of immunofluorescence staining for BrdU/SOX1, BrdU/TUJ1 (**A**), and CTIP2/SATB2 (**B**) in the mouse embryonic cortex (E18.5) from three groups: *Mark2*$^{+/+}$ mice (WT=4), untreated *Mark2*$^{+/-}$ mice (HET=4) and LiCl-treated () *Mark2*$^{+/-}$ mice (HET+LiCl=4), L1, L2-4, L5, L6 and IZ were marked to point out layers 1-6 and intermediate zone of mouse neocortex. Thick red dotted line was used to point out the CTIP2^{+} layer in L2-4, and thick green dotted lines was used to point out the SATB2^{+} layer, and thin red dotted line was used to point out the border of L6 with farthest CTIP2^{+} cells located. **D-I,** Quantification analysis of the data **in A-B,** including the numbers of SOX1^{+} cells (**D**), BrdU^{+} cells (**C**), TUJ1^{+} cells (**E**), thickness of CTIP2^{+} layer (**F,** thick red dotted line), SATB2^{+} layer thickness (**G,** thick green dotted line), proportion of CTIP2^{+} cells (**H**), and proportion of SATB2^{+} cells (**I**). The data of at least three independent experiments were analyzed by Student's t test; **p*<0.05, and ***p*<0.01. ns: not significant. scale bar = 50 μm.

METHODS

Behavioral and memory tests

All mice used for the behavioral tests were male mice aged 8-12 weeks (n≥8 per group), and all tests were performed between 09:00 and 17:00. Videos of the behavioral tests were analyzed by EthoVision XT 14 (Noldus).

Open field test

The open field test was conducted in a 50 x 50 x 50 cm box. A test subject was placed in the center of the box, and its behavior was video recorded for 5 min by a camera positioned directly above the box. Total distance and speed were quantified during video recording. A 30 cm square was delineated as the center zone.

Elevated plus maze test

Each mouse was placed in the central area of the elevated plus maze facing one of the open arms. The mice were allowed to explore the maze for 5 min, and the time spent in the open arm was calculated with EthoVision XT 14.

Three-chamber test

Two weeks before testing, subject animals and stimulus animals (female C57BL/6 mice aged 3-4 months) were housed alone in individual clean cages in the testing room. The test was performed in a novel, clean box (72 cm length x 72 cm width x 36 cm height) during the light phase. A subject mouse was placed in the empty apparatus and allowed to habituate to the three chambers, which contained two transparent bottles with holes (9 cm in diameter, 12 cm high), for 15 min. After habituation, one female stimulus mouse was placed in one of the transparent bottles in the right chamber, and the subject mouse was placed in the middle chamber and allowed to explore for 15 min. The subject mouse was then returned to its home cage. Then, another unknown female mouse was placed in the bottle in the other chamber (left) of the test box; the subject mouse was placed back in the test box equidistant from and facing the familiar and novel female mice. Interactions between the subject mouse with the familiar and novel female mice were videotaped for 15 min. Sniffing times were recorded and analyzed.

Novel object recognition test

A mouse was placed as in an open field test arena facing a wall and allowed to freely explore for 5 min. After a short rest in its home cage, the mouse was placed in the box again facing two identical objects (5 cm away from the walls) and allowed to explore for another 10 min exploration (T1). After a 60-min rest period, the mouse was placed in the box again facing two objects (a novel one and one that was present in T1) and allowed to explore for another 10 min (T2). The recognition index was calculated and analyzed.

Marble-burying test

Mice were individually placed in Plexiglas cages containing 5-cm-deep fresh bedding, and then 20 black glass marbles (15 mm diameter) were gently placed in a 4 x 5 arrangement at equal distances. Testing was conducted for 30 min. After the test period, buried marbles were counted. Marbles were considered buried if at least one half was covered with bedding.

Grooming test

The grooming task consisted of 15 min of habituation followed immediately measurement of grooming behavior for 15 min. Mice were individually placed in novel Plexiglas cages (45 cm x 22 cm). The time spent grooming the genitals, tail, paw, leg, body and head was recorded in seconds.

Y-maze test

Mice were placed in one arm of the Y-maze apparatus (20 cm high, 50 cm long, and 10 cm wide at the bottom) and allowed to explore freely for 10 min. A correct spontaneous alternation was defined as the successive entry of a mouse into the three arms in overlapping triplet sets. The spontaneous alternation percentage (%) was calculated as the number of successive triplet sets (consecutive entries into three different arms)/total number of arm entries minus 2) x100.

Barnes maze test

The apparatus was a rotatable gray acrylic disc (1.22 m in diameter) elevated 0.58 m above the floor with 20 holes (5 cm diameter, 2 cm away from the edge) equally spaced along the perimeter. The apparatus was brightly lit (600 lux). Only one hole in the maze top led to a removable hiding box, which was situated directly below the escape hole. On the first day, a mouse was placed in a transparent cylindrical start chamber (10.5 cm), and 30 s after the onset of a buzzer sound (85 dB), the chamber was lifted, and the mouse was allowed to freely explore the maze. The trial ended when the mouse entered the hiding box or after 3 min had elapsed. Mice that did not find the hiding box by the end of the 3-min period were gently guided to the escape hole by the investigator. Immediately after the mouse entered the hiding box, the buzzer sound was turned off, and the mouse was allowed to stay in the hiding box for 1 min. On the second day, the mouse was placed in a black square-shaped start chamber (10.5 cm), and 15 s after the onset of a buzzer sound (85 dB), the chamber was lifted, and the mouse was allowed to freely explore the maze. The trial ended when the mouse entered the hiding box or after 2 min had elapsed. Immediately after the mouse entered the hiding box, the buzzer sound was turned off, and the mouse was allowed to stay in the hiding box for 1 min. The experiment was repeated three times for each mouse. The procedure performed on the second day was conducted twice on the third day. On the fifth day, the subjects were placed in a black square-shaped start chamber (10.5 cm), and 15 s after the onset of a buzzer sound (85 dB), the chamber was lifted, and the mouse was allowed to freely explore the maze. The trial ended when the mouse entered the hiding box or after 2 min had elapsed. Immediately after the mouse entered the hiding box, the buzzer sound was turned off. The movements of the animals in the maze were digitally recorded.

Morris water maze test

A 120 cm diameter, 45 cm deep Morris water maze was filled with water, which was made with nontoxic white paint, to a depth of 25 cm. An escape platform (diameter 13 cm) was hidden 1 cm beneath the surface of the water in the center of one of the quadrants of the water tank. Four extra-maze cues, i.e., different shapes, were placed at equal distances on the wall surrounding the water tank. The water temperature was adjusted to 21±1°C. The mice were trained to find the escape platform in four trials per day for 6 consecutive days. In each trial, a mouse was placed in a randomly chosen quadrant and allowed to swim for up to 1 min to find and climb on the platform. If it failed to find the platform within that time, it was guided to the escape platform and kept there for 15 s. A probe test was conducted 24 h after completion of training. In the probe test, the platform was removed from the pool, and behavior was recorded for 60 s. Latency to reach the platform and time spent in the platform quadrant were recorded.